

# CHARACTERIZATION OF SQUEEZE-CAST AIB<sub>12</sub>/AI AND AIB<sub>2</sub>/AI COMPOSITES

by

**Lilia Olaya-Luengas**

A thesis submitted in partial fulfillment of the requirements for the degree of

MASTER OF SCIENCE

in

MECHANICAL ENGINEERING

UNIVERSITY OF PUERTO RICO  
MAYAGÜEZ CAMPUS  
2009

Approved by:

---

**Paul A. Sundaram**, Ph.D.  
Member, Graduate Committee

---

Date

---

**Jayanta Banerjee**, Ph.D.  
Member, Graduate Committee

---

Date

---

**O. Marcelo Suárez**, Ph.D.  
President, Graduate Committee

---

Date

---

**Felipe Acosta**, Ph.D.  
Representative of Graduate Studies

---

Date

---

**Ramón E. Vásquez**, Ph.D.  
ME Director Representative  
Dean of Engineering

---

Date

## **Abstract**

Aluminum alloys containing 2 and 4 wt.% copper reinforced with aluminum borides were successfully fabricated by squeeze casting employing squeezing pressures up to 62 MPa. The distribution of reinforcements in the composites was measured and the effect of pressure on density and hardness of the composites was determined. Additionally, the borides chemical stability was analyzed when the squeezed composites were heat treated. The pressure effect on the squeezed composites was investigated by optical microscopy, Vickers microhardness testing, superficial Rockwell hardness testing, differential thermal analysis (DTA) and high temperature X-ray diffraction (XRD). The superficial hardness of composites was considerably improved by increasing the applied pressure during squeeze cast process in comparison with specimens fabricated via gravity casting. The indirect squeeze cast technique caused  $\text{Al}_2\text{Cu}(\theta)$  phase segregation to upper regions of the specimens. A slight formation of  $\text{AlB}_2$  from the decomposition of the  $\text{AlB}_{12}$  was promoted during the annealing of squeezed composites.

## **Resumen**

Aleaciones de aluminio con 2 y 4 %peso de cobre reforzadas con  $\text{AlB}_{12}$  fueron fabricadas por la técnica indirecta de fundición por alta presión; con presiones desde 0.4 MPa hasta 62 MPa. En este proyecto se analizó la distribución de los refuerzos a lo largo del compuesto y se determinó el efecto de la presión sobre la densidad y la dureza del material. Además, la estabilidad del refuerzo fue determinada mientras el compuesto era tratado térmicamente. El efecto de la presión sobre el compuesto fue caracterizado por diversos métodos tales como microscopía óptica, microdureza Vickers, dureza superficial Rockwell, análisis termal diferencial y técnicas avanzadas de difracción de rayos X a alta temperatura. El incremento de la presión aplicada durante el proceso de fabricación, aumentó ligeramente la dureza superficial del compuesto; además, promovió la segregación de la fase  $\text{Al}_2\text{Cu}(\theta)$  a las regiones más altas del espécimen, por otra parte, las partículas de  $\text{AlB}_{12}$  permanecieron en las regiones bajas preferencialmente. La fase de  $\text{AlB}_{12}$  mostró una lenta formación de  $\text{AlB}_2$  promovida durante el recocido de los compuestos fabricados.

*To my mother  
by her words of strength  
and permanent support.*

## **Acknowledgments**

I want to express a sincere acknowledgement to my advisor, Dr. O. Marcelo Suárez because he gave me the opportunity to research under his guidance and supervision; to the University of Puerto Rico and Mechanical engineering program to let me improve my professional development.

I also want to thank the undergraduate students and my friends Elvin Estremera, Neysa Alicea, Lauren Muñoz and Erika Watts for their help in the design, development, and improving of squeeze casting technique and samples fabrication; special thanks to Josean J. Aponte for him unexhausted collaboration in manufacturing of squeeze casting attachments.

To **KB Alloys** for the donation of the Al-B master alloys.

To **National Science Foundation** for the grants N° DMR 0351449 (PREM Program) and N° CBET-0619349 (MRI Program) to provide the funding and the resources for the development of this research.

## Table of Contents

Abstract.....	ii
Resumen .....	iii
Acknowledgments.....	v
Table of Contents.....	vi
Table List .....	viii
Figure List.....	ix
1 INTRODUCTION .....	2
1.1 Motivation .....	3
1.2 Literature Review.....	5
1.3 What is lacking? .....	10
1.4 What is the relevance of the present work?.....	10
1.5 Objectives.....	11
1.5.1 Specific Objectives.....	11
1.6 Outline of the thesis.....	12
2 THEORETICAL BACKGROUND .....	14
2.1 Squeeze Casting .....	14
2.1.1 Process Outline.....	16
2.1.2 Process Variables .....	18
2.1.3 Effect of applied pressure .....	19
2.2 Metal Matrix Composites (MMCs) .....	21
2.3 Aluminum Matrix Composites (AMCs) .....	25
2.3.1 Al-Cu System .....	26
2.3.2 Al-B System .....	28
3 PROCESSING AND CHARACTERIZATION METHODOLOGY FOR FABRICATION OF AIB <sub>12</sub> /Al-Cu ALLOYS COMPOSITES .....	32
3.1 Squeeze Casting .....	32
3.2 Preparation of Samples .....	34
3.3 Characterization .....	35
3.3.1 Bulk Density .....	35

3.3.2	Microscopy Characterization .....	36
3.3.3	Vickers Microhardness .....	36
3.3.4	Analysis of Volume Fraction .....	37
3.3.5	Superficial Rockwell Hardness .....	37
3.3.6	Differential Thermal Analysis (DTA) .....	38
3.3.7	X-Ray Diffraction (XRD) .....	39
3.3.8	XRD + Differential Scanning Calorimeter (DSC) .....	40
3.3.9	High Temperature XRD .....	40
4	ANALYSIS AND DISCUSSION OF CHARACTERIZATION OF $\text{AlB}_{12}/\text{Al-Cu}$ ALLOYS COMPOSITES .....	42
4.1	Bulk Density .....	42
4.2	Microstructural Characterization .....	44
4.3	Analysis of Volume Fraction of $\text{Al}_2\text{Cu}$ and $\text{AlB}_{12}$ Phases .....	47
4.4	Vickers Microhardness .....	49
4.5	15T Superficial Rockwell Hardness .....	51
4.6	Differential Thermal Analysis (DTA) .....	52
4.7	X-Ray Diffraction (XRD) .....	57
4.7.1	XRD + Differential Scanning Calorimeter (DSC) .....	57
4.7.2	High Temperature XRD .....	60
5	CONCLUSIONS .....	66
	References .....	69
	Appendix .....	72

## Table List

Tables	Page
Table 2.1 Crystal data for the crystals of $\text{AlB}_2$ and $\alpha\text{-AlB}_{12}$ .....	31
Table 4.1 Comparative chart of melting point, solidification and liquidus line of reference.....	56
Table 4.2 Comparative chart of phase change (by heating and cooling) and solidus line of reference.....	54



## Figure List

Figures	Page
Figure 1.1 Outline of research methodology .....	13
Figure 2.1 Schematic diagram to illustrate the modes of the squeeze casting process .....	15
Figure 2.2 Schematic diagram to show two forms of the direct squeeze casting process. ....	15
Figure 2.3 Schematic illustrating squeeze casting process operations. ....	17
Figure 2.4 Classification scheme for the various composite types [17]. ....	21
Figure 2.5 The aluminum-copper phase diagram, showing the composition range for the 2xxx series .....	27
Figure 2.6 Al-rich side of Al-B phase diagram [4]. ....	29
Figure 2.7 Al-B phase diagram redrawn [24]. ....	30
Figure 3.1 Machining of mold.....	33
Figure 3.2 Cross section of system used for squeeze casting. ....	33
Figure 3.3 Press with special fixture. ....	34
Figure 3.4 (a) Squeezed Specimen. (b) Sectioned Specimen .....	35
Figure 3.5 XRD DSC chamber with a composite sample.....	40
Figure 3.6 Rigaku XRD executing a high temperature test. ....	41
Figure 4.1 Bulk Density of composite fabricated.....	43
Figure 4.2 Observed phases in composites.....	44
Figure 4.3 Optical micrographs from the bottom and top sections .....	45
Figure 4.4 Micrographs of cracks observed. ....	46
Figure 4.5 EDS analysis from BEI image to an $AlB_{12}$ particle. ....	47
Figure 4.6 Calculated volume fraction of $Al_2Cu$ and $AlB_{12}$ phases.....	48
Figure 4.7 Vickers microhardness (HV 25gf/30s) values measured on the matrices .....	50
Figure 4.8 Superficial Rockwell hardness (15T) values .....	51
Figure 4.9 Phase diagram Al-Cu.....	52
Figure 4.10 Phase change of all analyzed 4% Cu samples. ....	54
Figure 4.11 Eutectic phase observed in 4 wt% Cu samples. ....	54
Figure 4.12 DTA and 1 <sup>st</sup> Derivative curves of 4 wt.% specimen .....	55
Figure 4.13 Melting points of all analyzed samples.....	56
Figure 4.14 XRD Patterns of Al $2\theta=38.4^\circ$ (1 1 1) at 5 cm from specimen bottom .	57
Figure 4.15 $Al_2Cu$ peak increasing.....	58
Figure 4.16 $AlB_{12}$ peak increasing. ....	59

Figure 4.17	AlB <sub>2</sub> peak increasing.....	60
Figure 4.18	XRD patterns of cross section at 5 cm from bottom specimen .....	61
Figure 4.19	Al Peak at $2\theta=65.1^\circ$ of (2 0 0) .....	62
Figure 4.20	XRD patterns of cross section at 10 cm from bottom specimen .....	63
Figure 4.21	AlB <sub>12</sub> peak increasing. ....	64
Figure 4.22	AlB <sub>2</sub> peak increasing.....	65

# 1 INTRODUCTION

Aluminum matrix composites (AMCs) have found extensive use in many engineering applications because of their high specific modulus, strength, hardness and stiffness; excellent wear resistance, low-heat expansion coefficient, stability of properties at elevated temperature, reduced density and competitive fabrication cost. The development of these materials has been driven by the aerospace and automotive industries for both nonstructural and structural applications. In recent years the aerospace community has developed high-temperature aluminum alloys capable of competing with titanium alloys.

The present thesis is focused on the fabrication via indirect squeeze casting of aluminum-copper matrix composites reinforced with  $\text{AlB}_{12}$  particles. As a result, the main goal was to study the effect of squeeze pressures on the density, microhardness, hardness and thermal behavior of composites, as well as the distribution of  $\text{AlB}_{12}$  particles upon casting and resulting shrinkage porosity. To accomplish these goals this study includes the characterization of  $\text{Al}_2\text{Cu}$ ,  $\text{AlB}_{12}$  and  $\text{AlB}_2$  phases during annealing by *in situ* high temperature X-ray diffraction.

## **1.1 Motivation**

Casting is the most economical route to transfer raw materials into readily or almost readily usable components. However, one of the major drawbacks for conventional or even more advanced casting techniques, *e.g.*, high pressure die-casting is the formation of defects such as porosity. Furthermore, segregation defects of hot tears, A and V segregates and banding could be potential crack initiators during service operation of the as-cast components. New casting techniques have, therefore, been developed to compensate for these shortcomings. Of the many such casting techniques available, squeeze casting has greater potential to create less defective cast components [1]. Squeeze casting is now the most popular fabrication route for MMC artifacts. The annual 12-15% growth rate of MMCs in the automotive, aerospace, sports and leisure goods and other markets is a clear indication of better usage of advanced manufacturing routes such as squeeze casting [2].

Generally, the engineering components fabricated by squeeze casting are fine grained with excellent surface finish and have almost no porosity. They come in a variety of shapes and sizes. The mechanical properties of these parts are significantly improved over those of conventional castings and more sophisticated casting routes of pressure or gravity die-casting. With this technique, properties such as yield strength, elongation and fatigue strength can be improved; dimensional accuracy is similar to those of die-casting. It is further claimed that

components fabricated by squeeze casting have superior weldability and heat treatability. In addition, since squeeze casting may be carried out without any feeding system, runners, gates, etc., and shrinkage compensating units, risers, the yield is quite high with almost no scrap for recycling. Finally, in contrast to forging, squeeze cast components are fabricated in a single action operation with lesser energy requirements [1].

Aluminum–boron alloys have been used as additives to Al alloys to promote grain refinement, precipitation hardening and mechanical reinforcement of Al–Base alloys. In particular in the Al–B system, the  $\text{AlB}_{12}$  phase is a promising compound for high temperature thermoelectric application and aircraft protection [3]. Al–B master alloys are also used in the *in situ* fabrication of aluminum matrix composites. One example is the *in situ* fabrication of  $\text{AlB}_2$  fiber reinforced aluminum matrix composites using an Al–B master alloy [4].

AMCs reinforced with dodeborides have not been studied despite being strong and lightweight materials. AMCs combine the low density of the matrix with the high hardness of the reinforcements. For this reason extensive analysis and characterization of these AMCs are relevant if they are proposed as alternative materials for aerospace applications.

## **1.2 Literature Review**

The squeeze casting process was first suggested by Chernov in 1878 [1] and later it was introduced in the United States, Europe and Japan [5]. This process was introduced in the United States in 1960 and has since gained widespread acceptance within the nonferrous casting industry. Aluminum, magnesium and copper alloy components are manufactured using this process. Several ferrous components with relatively simple geometry have also been manufactured by squeeze casting [6].

Zhang *et al.* [7] reported the effect of applied pressure during squeeze casting process on microstructure and properties of the ZL205A alloy, which is a high-strength casting aluminum alloy (named under Chinese designation). This has been widely used for high-loaded structural parts. In this study, tensile strength and elongation of the alloy were increased with increasing applied pressure; however, the increase of tensile strength and elongation were apparent only at pressures less than 45 MPa and 75 MPa, respectively. The squeezing pressure had significant influence on the microstructure of the alloy; the grain size of the alloy decreased with the increase of the squeezing pressure. With increasing pressure, the amount of dimple on fractural surface increased, but the dimple size becomes smaller. Microporosity could be seen easily in the alloy when the alloy was cast with no applied pressure; as the squeezing pressure reached 25 MPa, the microporosity

could be rarely found and it disappeared completely with increasing squeezing pressure.

Maleki *et al.* [8] studied the effects of applied pressure, melt and die temperatures on the density, macrostructure and hardness of squeeze cast LM13 alloy, which is a heat treatable cast Al-Si alloy with good bearing properties, good fluidity and low coefficient of thermal expansion, commonly used for automotive parts. This research showed that the density of the samples decreased with a 20 MPa external pressure but it increased steadily for higher applied pressures up to about 106 MPa after which it became almost constant. Increasing the applied pressure resulted in smaller grain size and improved hardness.

Maeng *et al.* [9] have investigated the direct squeeze casting of B390 as a function of melt temperature and applied pressure. B390 alloy is a hypereutectic Al-Si alloy characterized by its high wear resistance, which is typically used in ring gears, engine blocks, pistons, etc. [10]. Mechanical properties such as hardness and tensile strengths were greatly improved with increasing applied pressure. This was due not only to the refinement of Chinese script microstructure but also to the increase in solubility of solute atoms and a decrease of interdendritic pores with the applied pressure.

Kajjari and Divandari [11] investigated the effect of pressure on the microstructure and reduction of shrinkage porosities and the effect of squeeze pressure (30, 50 and 70 MPa) on the microstructure and tensile properties of

AA2024 aluminum alloy. The results showed that squeeze casting caused the refinement of the microstructure and reduction in the dendrite arm spacing (DAS) of the cast structure possibly due to higher cooling rates. Increasing the squeeze pressure also led to formation of a finer microstructure. Furthermore, higher pressures decreased the percentage of porosity and increased the density of the cast alloy. The higher densities were found in the samples produced by squeeze casting, although the density difference between the samples cast at 50 and 70 MPa pressures is not appreciable. The ultimate tensile strengths of the squeezed cast samples improved when the squeeze pressure increased.

Youn and Kang [12] investigated the nano/microstructure of squeezed cast A356 alloy, the aging response (in T5 heat treatment), and the mechanical/tribological properties of the eutectic regions. This squeeze cast alloy (100 MPa) was used because no porosity was observed due to the well positioned overflows. Porosity not only reduces mechanical properties, but also interferes with heat treatment.

Some investigators have used composite materials fabricated via squeeze casting in their researches. Arhami *et al.* [13] investigated the effect of vanadium on the composition and morphology of intermetallics formed during the squeeze casting (80 MPa) of Mg modified Al–8Fe–1.4V–8Si alloy in both monolithic form and as-reinforced with SiC particles.



Li *et al.* [14] fabricated an  $(\text{Al}_3\text{Zr}+\text{Al}_2\text{O}_3)_p/\text{A356}$  particles reinforced aluminum matrix composite; the composite melt was cast via permanent mold and squeeze casting (65-80 MPa). One of the major drawbacks for the permanent mould casting was the formation of defects such as porosity. In the squeeze cast composites the defects were less pronounced and the grains were finer than those in permanent mold composite. Additionally, the tensile strength, elongation, abrasability and corrosion resistance of squeeze cast composite were enhanced. The improved properties of that composite were attributed to the high density and finer grain of the matrix obtained via squeeze casting.

Chen *et al.* [15] fabricated aluminum matrix composites reinforced with various levels and sizes of silicon carbide particles ( $\text{SiC}_p$ ) by squeeze casting (75 MPa). A lower melting point alloy (A383 Al) was squeezed into the higher melting point ( $\text{SiC}_p$ /pure Al) and ( $\text{SiC}_p$ /6061 Al) preforms. The results showed that the SiC particles were uniformly distributed within the matrices, and no pore was found in these composites. The tensile strengths and elongations of the  $\text{SiC}_p$ /pure Al/A383 Al and  $\text{SiC}_p$ /6061 Al/A383 Al composites were both better than those of the A383 Al alloy.

Jung *et al.* [16] developed a finite element model for the process of squeeze casting (25 MPa) of metal matrix composites in cylindrical molds. The squeeze-casting conditions directly influenced the MMC microstructure and the mechanical properties, so that it was important to determine the optimal processing conditions.

Trial and error procedure was used to develop new processes and optimize the processing parameters. This approach is expensive and is also inflexible in that the result cannot be adapted to other materials or shapes of mold. The model predicted the cooling behavior from the processing parameters of the casting process.

Vijayaram *et al.* [5] reviewed the principles of squeeze casting technology, which can be applied to process discontinuous fiber reinforced metal matrix composite castings. In addition, they highlighted the type of engineering components produced by this advanced casting method and concluded that the squeeze casting can be adopted to produce superior quality composite castings. The composite castings produced by this method were application-oriented products, which can be manufactured by mass production. They noted that the availability of the ceramic fiber performs in required size and shape favored and helped the production of composite castings and that it has a strong potential. The international and national market for squeeze cast components could not fully exploited by the industries due to the lack of commercially viable machines. They expected that this process fill up this gap and will become a harbinger for this emerging technology.

### **1.3 What is lacking?**

The analysis of the literature review revealed that although there are some researches which apply the squeeze casting, it is lacking an extensive research about the  $\text{AlB}_{12}/\text{Al}$  composites and the squeeze casting as a fabrication technique of composite materials. By this way the aluminum matrix composites could acquire the good properties that this technique offers.

Some projects deal already with the  $\text{AlB}_{12}/\text{Al}$  composites such as fabrication of composite by different cast methods as centrifugal casting, rapid solidification and squeeze casting. An exhaustive characterization of Aluminum matrix composite reinforced with  $\text{AlB}_{12}$  particles, an analysis of the chemical stability of  $\text{AlB}_{12}$  as reinforcement, determine the melting point of composites and analyze their possible changes from as-casting composites and study the increase or decrease of each one of the phases present in composite by X-ray diffraction during heat treatments could be executed.

### **1.4 What is the relevance of the present work?**

The relevance of the present project is the fabrication of  $\text{AlB}_{12}/\text{Al}$  composites by indirect squeeze casting method with several squeeze pressure, a moderate improvement of mechanical behavior such as microhardness, hardness and bulk density of squeezed  $\text{AlB}_{12}/\text{Al}$  composite. A slight segregation of  $\text{Al}_2\text{Cu}$  phase to

upper regions of squeezed samples was observed and quantified by optical microscopy and volume fraction respectively. Besides, the elastic modulus of the composite material was calculated from volume fraction calculated.

The characterization of  $\text{AlB}_{12}/\text{Al}$  composites was accomplished by determining the melting point of squeeze-composites with the help of differential thermal analysis (DTA) and comparing with as-casting composites. Finally, a tracking of peaks of  $\text{Al}_2\text{Cu}$  and  $\text{AlB}_{12}$  phases presented in squeeze-composites was carried out by high temperature x-ray diffraction techniques.

## **1.5 Objectives**

To fabricate and characterize aluminum-copper matrix composites reinforced with  $\text{AlB}_{12}$  particles by squeeze casting technique.

### **1.5.1 Specific Objectives**

- ♦ To design the squeeze casting prototype machine where the composite samples will be fabricated and to determine the optimum parameters for its operation, such as preheating temperature for mold, applied pressure and casting temperature.

- ♦ To characterize the squeeze casting composites using optical microscopy and scanning electron microscopy (SEM) with backscattered electron imaging capabilities for determining the phases present and microstructure.
- ♦ To calculate the volume fraction and distribution of reinforcement from optical photographs of microstructures using ImageJ image analysis software and to find the elastic modulus of composite using that information.
- ♦ To determine the phases present in the composites by means of X-ray diffraction (XRD) and to determine the stability of these phases upon heat treatment using high temperature XRD.
- ♦ To measure the superficial hardness and to calculate the Meyer hardness of composites in order to observe the changes of mechanical behavior when these materials are fabricated via squeeze casting.

## **1.6 Outline of the thesis**

Chapter 2 deals with the theory of squeeze casting process, and a critical summary on the metal matrix composites, aluminum matrix composites and the binary systems involved in the present research like Al-Cu and Al-B. Third chapter presents the complete procedure, as well as design and manufacture of the mold-piston system for squeeze casting process. The squeeze casting variables setting and sample preparation for each characterization technique are also discussed.

Fourth chapter presents the characterization process, the data analysis and the discussion of those results. Finally, the chapter 5 includes the conclusions of the present research.

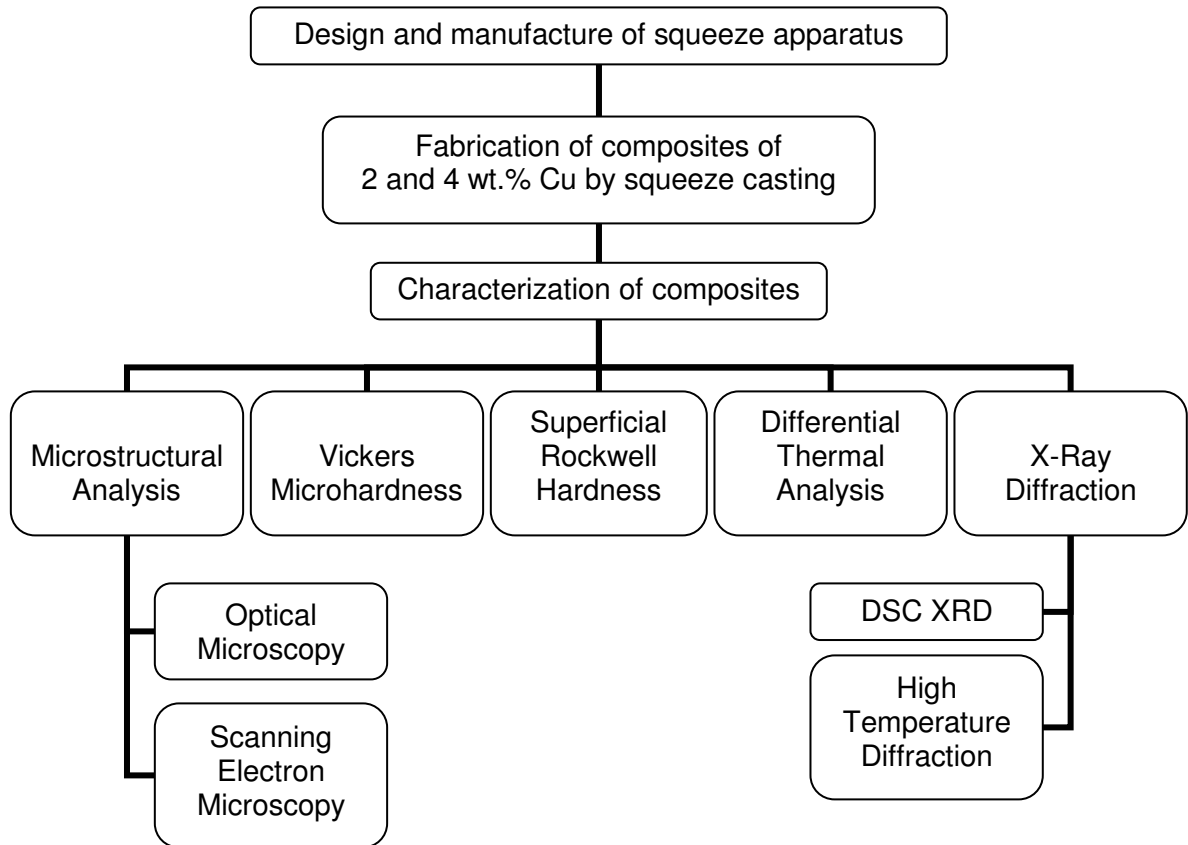


Figure 1.1 Outline of research methodology

## **2 THEORETICAL BACKGROUND**

### **2.1 Squeeze Casting**

Squeeze casting is a generic term to specify a fabrication technique where solidification is promoted under high pressure within a re-usable die. Squeeze casting consists of metering liquid metal into a preheated, lubricated die and forging the metal while it solidifies. The load is applied shortly after the metal begins to freeze and is maintained until the entire casting has solidified. Casting ejection and handling are done in much the same way as in closed die forging [6].

Although squeeze casting is now the accepted term for this forming operation, it has been variously referred to as “liquid metal forging” [6], “extrusion casting”, “liquid pressing”, “pressure crystallization” and “squeeze forming”. Two basic forms of the process may be distinguished, depending on whether the pressure is applied directly onto the solidifying cast product via an upper or male die (punch) or the applied pressure is exerted through an intermediate feeding system, as schematically shown in Figure 2.1: the direct and indirect squeeze casting modes. For the direct mode, two further forms may be distinguished, based on liquid metal displacement initiated by the punch movement: (a) without metal movement, and (b) with metal movement. As illustrated in Figure 2.2, the first form is suitable for ingot

type components where there is no metal movement, while the second type involving metal movement (also known as the backward process), is more versatile and can be used to cast a wide range of shaped components [1]. In indirect squeeze casting process, the metal is injected into the die cavity by a piston of small diameter [7].

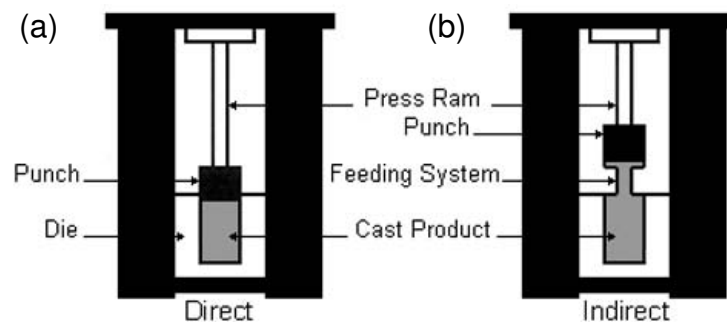


Figure 2.1 Schematic diagram to illustrate the modes of the squeeze casting process (a) direct and (b) indirect [1].

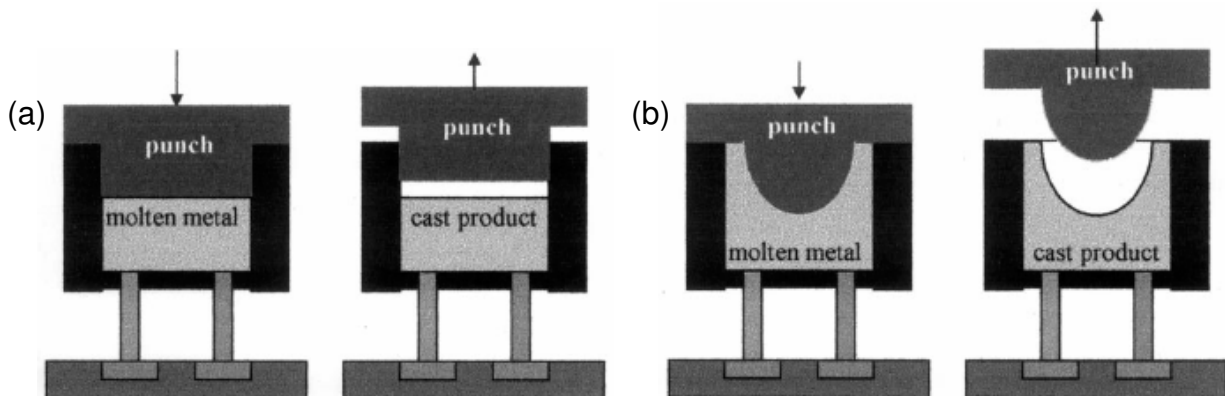


Figure 2.2 Schematic diagram to show two forms of the direct squeeze casting process. a) without metal movement. b) with metal movement [1].



### **2.1.1 Process Outline**

The process of squeeze casting involves the following steps [1]:

1. A pre-specified amount of molten metal is poured into a preheated, lubricated die cavity, located on the bed of a hydraulic press, as shown in Figure 2.3 (a) and (b).
2. The press is activated with pressures of up to 140 MPa [6] to close the die cavity and to pressurize the liquid metal. This is carried out very quickly, rendering solidification of the molten metal under pressure.
3. The pressure is held on the metal until complete solidification. This not only increases the rate of heat flow, but also most importantly may eliminate macro/micro shrinkage porosity. In addition, since nucleation of gas porosity is pressure dependent, the porosity formation due to dissolve gases in the molten metal is restricted, as indicated in Figure 2.3 (c).
4. Finally, Figure 2.3 (d) shows the casting ejection and handling done in much the same way as in closed die forging.

The squeeze casting cycle starts with the transfer of a metered quantity of molten metal into the bottom half of a preheated die set mounted in a hydraulic press. The dies are then closed, and this fills the die cavity with molten metal and applies pressures of up to 140 MPa on the solidifying casting.

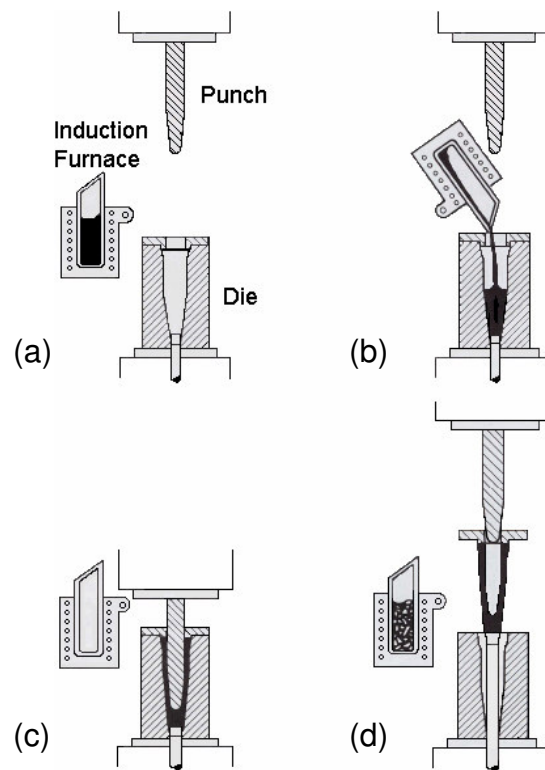


Figure 2.3 Schematic illustrating squeeze casting process operations.  
(a) Melt charge, preheat and lubricate tooling. (b) Transfer melt into die cavity. (c) Close tooling, solidified melt under pressure. (d) Eject casting, clean dies, charge melt stock [6].

The high pressure applied (typically 55 to 100 MPa) is enough to suppress gas porosity except in extreme cases, for which standard degassing treatments are used. The tendency toward shrinkage porosity is limited by using minimal superheat in the melt during pouring. This is possible in squeeze casting because of melt fluidity, which requires high pouring temperatures, and is not necessary to fill the die, the latter being readily achieved by the high pressure applied. In heavy sections of the casting, which are particularly prone to the incidence of shrinkage porosity, the applied pressure squirts liquid or semiliquid metal from hot spots into incipient shrinkage pores to prevent pores from forming. Alloys with wide freezing ranges

accommodate this form of melt movement very well, resulting in sound casting with a minimum of applied pressure [6].

### **2.1.2 Process Variables**

There are a number of variables that are generally controlled for the soundness and quality of the castings. The variable ranges discussed in the following sections vary with the alloy systems and part geometry being squeeze cast [6]:

- ♦ **Melt volume:** precision control of the metal volume is required when filling the die cavity. This ensures dimensional control.
- ♦ **Casting temperatures** depend of the alloy and the part geometry. The starting point is normally 6 to 55 °C above the liquidus temperature.
- ♦ **Tooling temperatures** ranging from 190 to 315 °C are normally used. The lower range is more suitable for thick section casting. The punch temperature is kept from 15 to 30 °C below the lower die temperature to maintain sufficient clearance between them for adequate venting. Excess punch-to-die clearance allows molten metal to be extruded between them eroding the surface.
- ♦ **Time delay** is the duration between the actual pouring of the metal and the instant the punch contacts the molten pool and then starts the pressurization of thin webs that are incorporated into the die cavity. Because increased pouring temperatures may be required to fill adequately these sections upon pouring, a

time delay will allow for cooling of the molten pool before closing of the dies in order to avoid shrink porosity.

- ♦ **Pressure levels** of 50 to 140 MPa are normally used; 70 MPa is generally applied, depending on part geometry and the required mechanical properties. There is an optimum pressure for each system after which no added advantages in mechanical properties are obtained.
- ♦ **Pressure duration** varying from 30 to 120 seconds has been found to be satisfactory for casting weighing 9 Kg. However, the pressure duration is again dependent on part geometry. Applied pressure after composite solidification and temperature equalization will not enhance any property; it will only increase cycle times.
- ♦ **Lubrication** for aluminum, magnesium and copper alloys has been proved satisfactorily with a colloidal graphite spray lubricant applied on the warm dies prior to casting. Care should be taken to avoid excess buildup on narrow webs and fin areas where vent holes or slots are used. Care must also be taken to prevent plugging of these vents. For ferrous castings, ceramic-type coatings are required to prevent welding between the casting and the metal die surfaces.

### **2.1.3 Effect of applied pressure**

Application of pressure on a molten metal during solidification may cause the following effects [8]:

- ♦ **Change in the melting point.** Melting point (liquidus temperature) of most metals and alloys increases under pressure, to satisfy the Clausius–Clapeyron equation. This characteristic can be utilized to create sudden large undercooling in the melt upon application of pressure if the melt temperature and timing of pressure application are accurately controlled.
- ♦ **Change of solidification rate.** In most casting processes an air gap is formed shortly after pouring between the die and the solidified outer shell of the casting. This is due to simultaneous contraction of the shell and expansion of the die. Air gap formation changes heat transfer mechanism from conduction to convection and radiation and causes a significant decrease in heat transfer rate and consequently decreases the cooling rate. In squeeze casting, air gap formation is eliminated as a result of the applied pressure on the casting and therefore heat transfer and cooling rate increases considerably. Higher cooling rate, especially if coupled with a prompt large undercooling as mentioned above, can cause significant improvement in the structure and mechanical properties of the castings.
- ♦ **Structural changes.** Applied pressure causes structural changes by affecting cooling rate of the melt and its undercooling. These structural changes include decrease in dendrite arm spacing (DAS), more homogeneous distribution of structural features and refinement and modification of intermetallic phases. These factors cause improvement in the mechanical properties of squeeze cast components.

- ♦ **Reduction of gas and shrinkage porosities.** It has been shown that gas solubility in the melt increases under an applied pressure. This makes gas bubble nucleation more difficult. It is also well established that application of an external pressure during solidification of a casting activates the different feeding mechanisms and hinders shrinkage porosity formation. Consequently, if a high enough pressure is used, formation of both gas and shrinkage porosities may be completely eliminated.

## 2.2 Metal Matrix Composites (MMCs)

One simple scheme for the classification of composite materials is shown in

Figure 2.4, which consists of three main divisions: particle-reinforced, fiber reinforced, and structural composites; also, at least two subdivisions exist for each. The dispersed phase for particle-reinforced composites is equiaxed; for fiber-reinforced composites, the dispersed phase has the geometry of a fiber. Structural composites are combinations of composites and homogeneous materials.

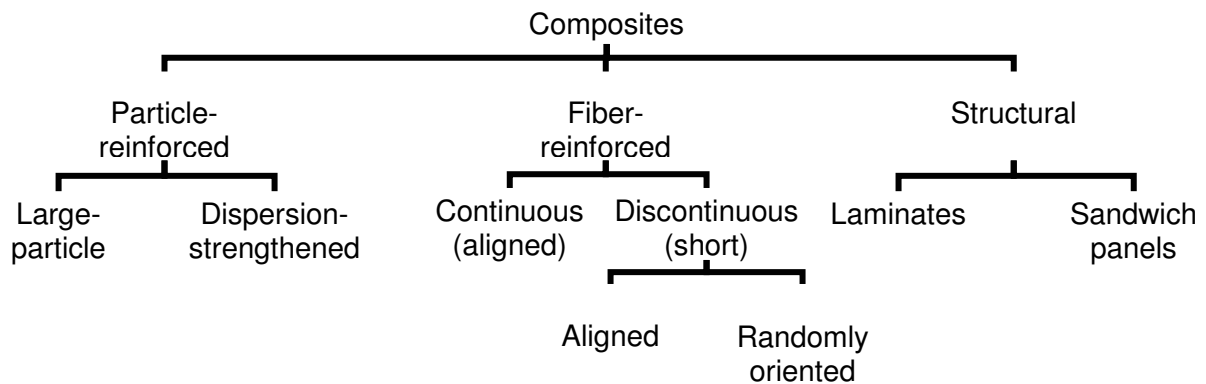


Figure 2.4 Classification scheme for the various composite types [17].

The large-particle and dispersion-strengthened composites are the two subclassifications of particle-reinforced composites. The distinction between these is based upon reinforcement or strengthening mechanism. The term “large” is used to indicate that particle-matrix interactions cannot be treated on the atomic or molecular level; rather, a continuum mechanics configuration is used. For the most of these composites, the dispersed phase is harder and stiffer than the matrix. These reinforcing particles tend to restrain movement of the matrix phase in the vicinity of each particle. In essence, the matrix transfers some of the applied stress to the particles, which bear a fraction of load. The degree of reinforcement or improvement of mechanical behavior depends on strong bonding at the matrix-particle interface. For dispersion-strengthened composites, particles are normally much smaller, with a size range between 0.01 and 0.1  $\mu\text{m}$ .

In large-particle composite, particles can have quite a variety of geometry, but they should be equiaxed. For effective reinforcement, the particles should be small and evenly distributed throughout the matrix. Furthermore, the volume fraction of the two phases influences the behavior; mechanical properties are enhanced with increasing particle content. Two mathematical expressions have been formulated for the dependence of the elastic modulus on the volume fraction of the constituent phases for a two-phase composite. These rule of mixtures equations predict that the elastic modulus should fall between an upper bound represented by

$$E_c(u) = E_m V_m + E_p V_p \quad \text{Equation 2.1}$$

and a lower bound, or limit,

$$E_c(l) = \frac{E_m E_p}{E_m V_p + E_p V_m} \quad \text{Equation 2.2}$$

In these expressions, E and V denote the elastic modulus and volume fraction, whereas the subscriptions c, m and p represent composite, matrix and particulate phases respectively [17].

Normally for the MMCs, the matrix is a ductile metal. These materials may be utilized at higher service temperatures than their base metal counterparts; the reinforcement may improve specific stiffness, specific strength, abrasion resistance, creep resistance, thermal conductivity, and dimensional stability. Some of the advantages of these materials over the polymer-matrix composites include higher operating temperatures, non-flammability, and greater resistance to degradation by organic fluids. Metal matrix composites are much more expensive than polymer matrix composites, and therefore, their (MMCs) use is somewhat restricted.

Superalloys, as well as alloys of aluminum, magnesium, titanium and copper, are employed as composite matrix. The reinforcement may be in the form of particulates, both continuous and discontinuous fibers, and whiskers; concentrations normally range between 10 and 60 vol%. Continuous fiber materials include carbon, silicon carbide, boron, aluminum oxide, and the refractory metals. On the other hand, discontinuous reinforcements consist primarily of silicon carbide whiskers,



chopped fibers of aluminum oxide and carbon, and particulates of silicon carbide and aluminum oxide. In a sense cermets fall within this MMCs scheme.

Some matrix-reinforcement combinations are highly reactive at elevated temperatures. Consequently, composite degradation may be caused by high-temperature processing or by subjecting the MMCs to elevated temperatures during service. This problem is commonly resolved either by applying a protective surface coating to the reinforcement or by modifying the matrix alloys composition.

Normally the processing of MMCs involves at least two steps: consolidation or synthesis, followed by a shaping operation. A host of consolidation techniques are available, some of which are relatively sophisticated; discontinuous fiber MMCs are amenable to shaping by standard metal-forming operations (e.g., forging, extrusion, rolling).

Automobile manufacturers have recently begun to use MMCs in their products. For example, some engine components have been introduced consisting of an aluminum-alloy matrix that is reinforced with aluminum oxide and carbon fibers; this MMCs is light in weight and resists wear and thermal distortion. Metal matrix composites are also employed in driveshafts (that have higher rotational speed and reduced vibrational noise levels), extruded stabilizer bars, and forged suspension and transmission components.

The aerospace industry also uses MMCs. Structural applications include advanced aluminum alloy metal-matrix composites; boron fibers are used as the reinforcement for the Space Shuttle Orbiter, and continuous graphite fibers for the Hubble Telescope [17].

Pressure infiltration of fiber preforms or powder beds are used in order to produce void-free, near-net shape casting of composites. Aluminosilicate fiber reinforced aluminum alloy pistons made by a Japanese automaker have been in use in heavy diesel engines for some years, and a considerable amount of work has been done on the pressure casting of ceramic particle and fiber-reinforced MMCs for industrial applications [18].

## **2.3 Aluminum Matrix Composites (AMCs)**

Aluminum (Al)-based metal matrix composites (MMCs) make up a distinct category of advanced engineering materials that provide unique advantages over conventional Al alloys. Aluminum matrix composites have been used in different fields where low weight and thermal stability are key requirements. Typical applications include aerospace components, electronic packaging, high precision instrumentation, and automobile engine components [19]. At present, aluminum alloy matrix composites (AMCs) are finding applications in automotive sector and strategic sectors such as defense and aerospace, as well as in different segments of other engineering industries [20]. The 6061 and 7015 aluminum alloys are used in

the automotive industries (trucks, rail-road cars), towers and structural applications, furniture, pipelines, canoes and other applications where strength, weldability and corrosion resistance are needed [21].

Particle-reinforced AMCs represent an appealing alternative as an advanced material due to their high specific heat capacity and thermal conductivity as well as low density, high specific strength, high specific stiffness, controlled coefficient of expansion, fatigue resistance and superior dimensional stability. AMCs with excellent properties are tailor-made with different manufacturing methods like powder metallurgy, liquid metal infiltration, squeeze casting, etc. [22]

Extensive theoretical and experimental studies have been carried out on the fundamental relationships between the mechanical properties and the microstructure of AMCs with different types of matrix and either particles or fibers as reinforcement. The selection of the reinforcement type, geometry and volume fraction is critical to obtain the best combination of properties at a low cost. The particles used for reinforcement include: nitrides, borides, carbides and oxides [21].

### **2.3.1 Al-Cu System**

An alloy system of ample commercial importance is aluminum-copper. Although the phase diagram of this system is fairly complicated (see Figure 2.5), the alloys of concern in this discussion are limited to the Al-rich region where a simple  $\alpha\text{Al} + \text{Al}_2\text{Cu}$  ( $\theta$ ) eutectic is formed. The Al-Cu based alloys (designated as 2xxx

series) has nominal copper contents ranging from 2.3 to 6.3 wt.%, making them hypoeutectic alloys.

A critical feature of this region of the diagram is the curvature of the solvus line. At the eutectic temperature (548.2°C), 5.65 wt.% Cu will dissolve in aluminum. At lower temperature, however, the amount of copper that can remain in the aluminum solid solution under equilibrium conditions drastically decreases, reaching less than 1% at room temperature. This is the typical shape of the solvus line for precipitation hardening; if any of these alloys are homogenized at temperature in or near the solid solution phase field, they can be strengthened by aging at a substantially lower temperature [23].

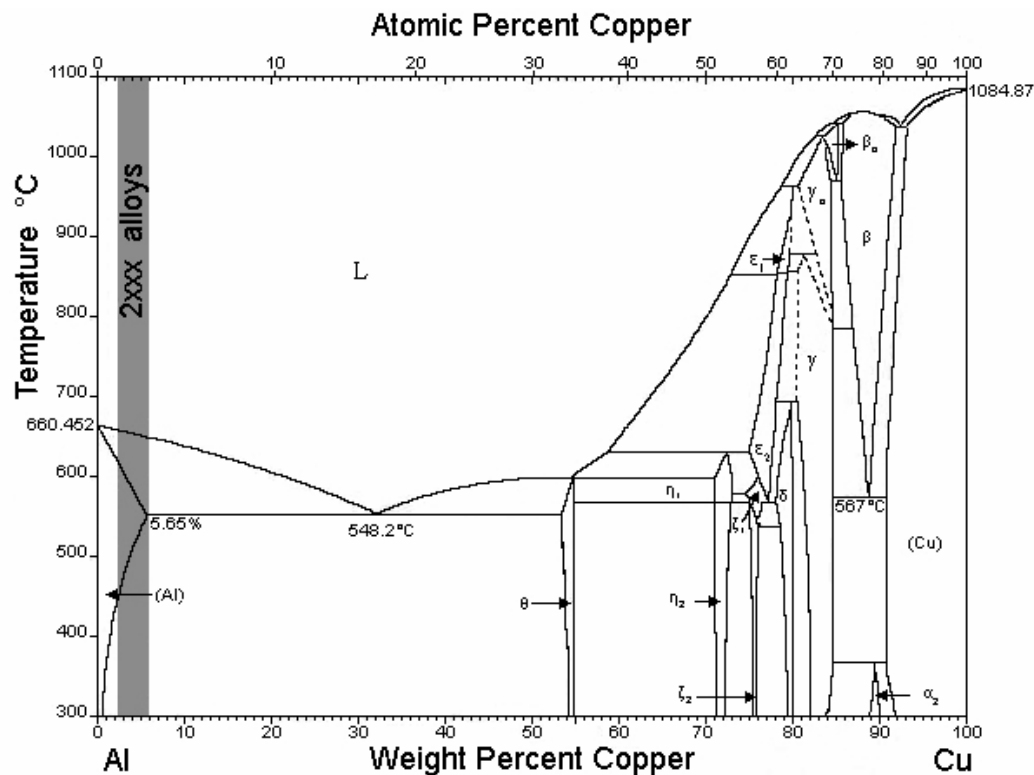


Figure 2.5 The aluminum-copper phase diagram, showing the composition range for the 2xxx series of precipitation-hardenable aluminum alloys [23].

### **2.3.2 Al-B System**

Commercial Al–B alloys are produced via chemical reactions of  $\text{KBF}_4$  with molten aluminum. Boron is reduced from the fluoride salt by aluminum and disperses into the aluminum melt in the forms of aluminum borides,  $\text{AlB}_2$  and  $\text{AlB}_{12}$ .  $\text{AlB}_{12}$  is a high temperature phase, whereas  $\text{AlB}_2$  is stable at room temperature when the boron content is less than 44.5 wt.%, according to the Al–B phase diagram, shown in Figure 2.6. According to the phase diagram Figure 2.6, a peritectic reaction,  $\text{L} + \text{AlB}_{12} \rightarrow \text{AlB}_2$ , takes place at 975°C. There is a discrepancy about the peritectic temperature, which has been given in different numbers by different investigators ranging from 956°C to 1350°C. During cooling  $\text{AlB}_{12}$  reacts with liquid aluminum to form  $\text{AlB}_2$ . However,  $\text{AlB}_{12}$  is always detected in Al–B master alloys that have been produced via molten salt reactions at temperatures lower than the peritectic reaction temperature for high boron concentrations. The presence of  $\text{AlB}_{12}$  was also reported in Al–Ti–B master alloys that have been produced via arc melting of aluminum and boron at 800°C. The presence of  $\text{AlB}_{12}$  at temperatures lower than 975°C continues causing confusion regarding the stabilities of the boride phases in aluminum [4].

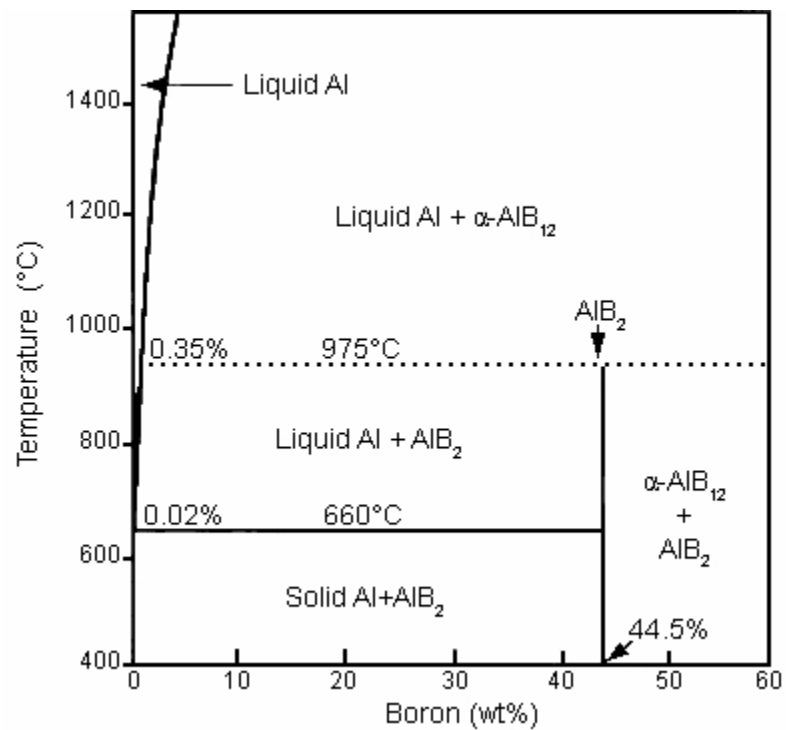


Figure 2.6 Al-rich side of Al-B phase diagram [4].

Recent researches [24] had reported an Al-B phase diagram redrawn [25]. However, it was pointed out that the diagram was unlikely two segments of AlB<sub>12</sub> liquidus, which were separated by the existence of AlB<sub>10</sub>, could not be smoothly continuous. Duschanek and Rogl reassessed this system and concluded that AlB<sub>10</sub> did not exist [25]. Mirković, D. *et al.* measured the AlB<sub>12</sub> liquidus and determined the form by thermodynamic assessment [3]. The result is shown in Figure 2.7.

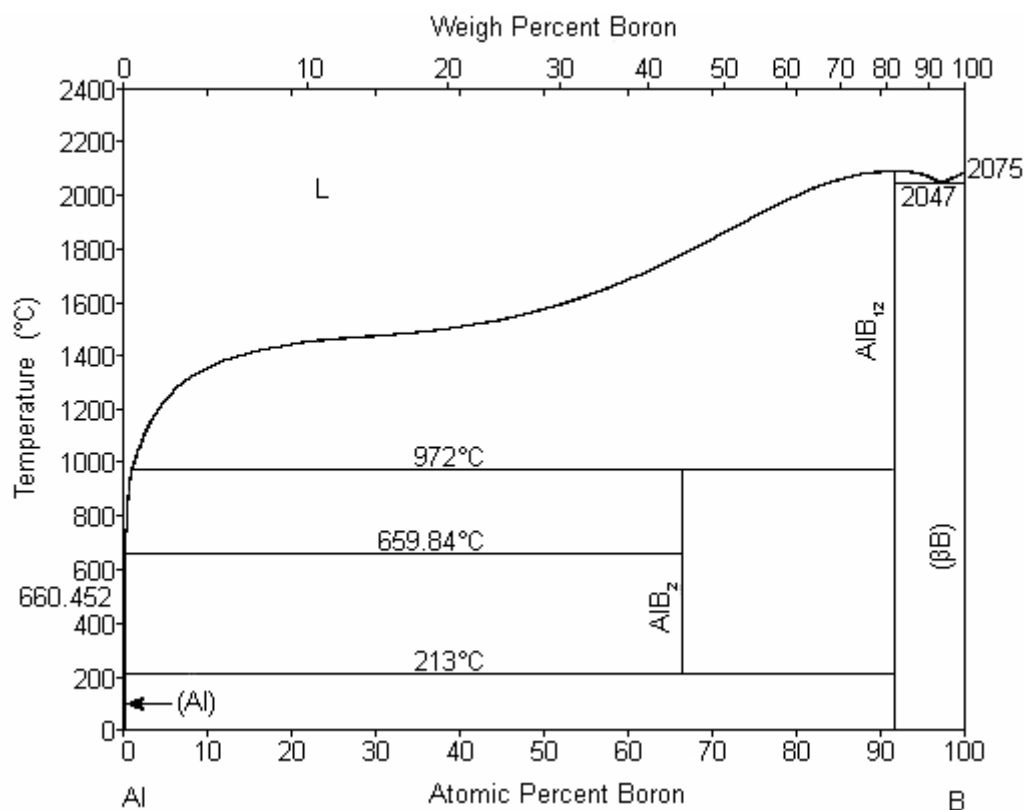


Figure 2.7 Al-B phase diagram redrawn [24].

According to Higashi, in the binary Al-B system only three phases,  $\text{AlB}_2$ ,  $\alpha\text{-AlB}_{12}$ , and (with less confidence)  $\gamma\text{-AlB}_{12}$ , are considered to be binary aluminum borides. The phases  $\text{AlB}_{10}$  and  $\beta\text{-AlB}_{12}$  may have been stabilized by carbon impurity. The  $\gamma\text{-AlB}_{12}$  could not be prepared as single crystals but as intergrown crystals with  $\alpha\text{-AlB}_{12}$  [26]. Although, Duschanek and Rogl [25] concluded that  $\alpha\text{-AlB}_{12}$  and  $\text{AlB}_2$  are the only true binary aluminum boride compounds, Table 2.1 shows the crystal data for both phases.

Table 2.1 Crystal data for the crystals of  $\text{AlB}_2$  and  $\alpha\text{-AlB}_{12}$

Crystal	$\text{AlB}_2$ [27]	$\alpha\text{-AlB}_{12}$ [26]
Crystal system	Hexagonal	Tetragonal
a(Å)	3.0054	10.158
b(Å)	(=a)	(=a)
c(Å)	3.25276	14.270
Chemical formula	$\text{AlB}_2$	$\text{B}_{22}\text{Al}_{1.6}$
Pearson Symbol [25]	$hP3$	$P6/mmm$
Space Group [25]	$tP216$	$P4_12_12$
Density [28]	$3.1 \text{ g/cm}^3$	$2.55 \text{ g/cm}^3$
Hardness [29]		26 GPa



### **3 PROCESSING AND CHARACTERIZATION METHODOLOGY FOR FABRICATION OF $\text{AlB}_{12}$ /Al-Cu ALLOYS COMPOSITES**

This chapter presents the methodology used to fabricate Al-Cu alloys reinforced with  $\text{AlB}_{12}$  particles via squeeze casting, and the corresponding characterization methods. To produce these aluminum matrix composites an Al-5 wt.% B and Al-33 wt.% Cu commercial master alloys were used.

#### **3.1 Squeeze Casting**

Two sets of Al matrix composite specimens were fabricated via squeeze casting with different squeeze pressures. The first set contained 2 wt.% Cu and 4.70 wt.% B and the second set, 4 wt.% Cu and 4.40 wt.% B. In both composites boron was present forming  $\text{AlB}_{12}$  particles.

A Romanoff electric furnace with a graphite crucible was used to melt the composites; the melted composite was kept at 750 °C for 30 min. After melting, the material was squeezed cast in an apparatus made of a stainless steel mold and a piston system. These mold and piston were machined and assembled according to Figure 3.1 and Figure 3.2 respectively.



Figure 3.1 Machining of mold

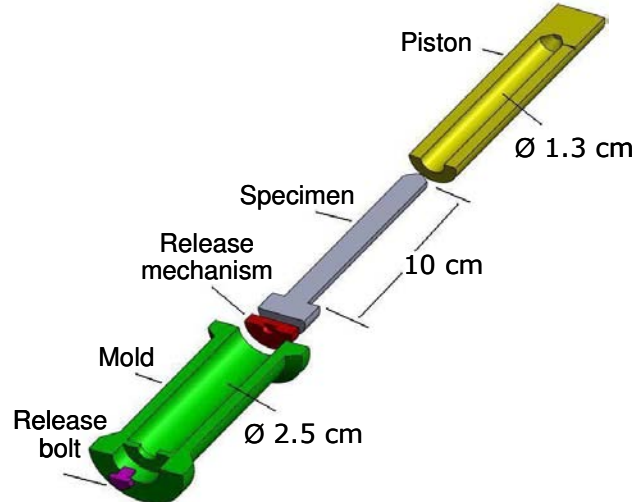


Figure 3.2 Cross section of system used for squeeze casting.

The stainless steel mold and hollow piston were coated with dry graphite lubricant and pre-heated in a Barnstead Thermolyte muffle furnace at 660 °C. The molten composite matrix with solid  $\text{AlB}_{12}$  particles in suspension was poured into the stainless steel mold. Before the matrix started solidifying near 660 °C, pressure was applied with the stainless steel hollow piston during the solidification process. The applied pressures on the specimens ranged from 0.40 MPa to 62 MPa using a

Carver hydraulic press furnished with a special fixture fabricated to enlarge the press gap (Figure 3.3).

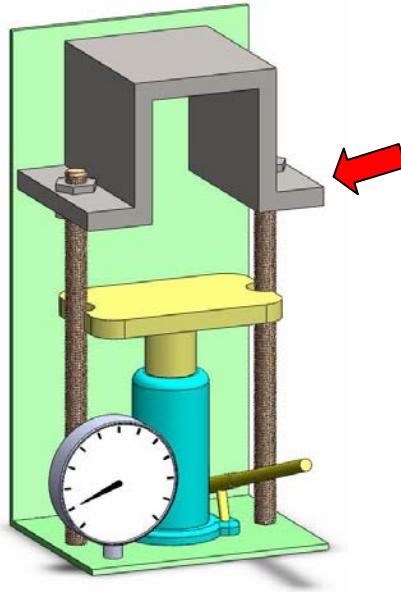


Figure 3.3 Press with special fixture.

## **3.2 Preparation of Samples**

The mold containing the solidified specimen was air cooled. The fabricated specimen was removed using the same press. Each cylindrical specimen obtained from the squeeze casting process were 13 mm in diameter and 11 cm in length; the specimens were cut to produce 5 cross sections along the squeeze casting direction, as shown in Figure 3.4. This longitudinal mapping of the squeeze cast piece allowed selecting the zones to be characterized. The cuttings of specimens were done with an Allied High Tech high speed saw. All cut samples were analyzed by optical microscopy, scanning electron microscopy, Vickers microhardness, superficial Rockwell hardness, differential thermal analysis and x-ray diffraction.

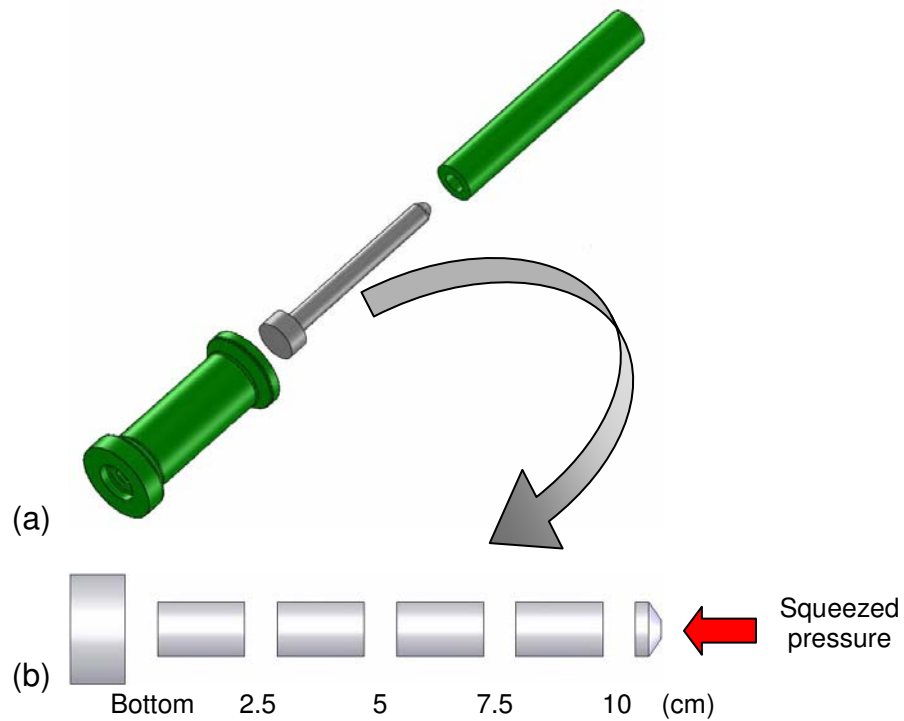


Figure 3.4 (a) Squeezed Specimen. (b) Sectioned Specimen

### 3.3 Characterization

#### 3.3.1 Bulk Density

Specific gravity was measured using a Sartorius TE 212 scale furnished with Sartorius YDK 01 density determination kit. Density is then calculated from specific gravity following ASTM D 792-08 “Standard Test Methods for Density and Specific Gravity (Relative Density) of Plastics by Displacement” [30].

### **3.3.2 Microscopy Characterization**

The whole metallographic procedure was carefully documented for reproducibility purposes. All samples were mounted in epoxy resin. Grinding was carried out with a series of 320, 400, 600, 800 and 1200 grit SiC paper using water as the coolant/lubricant. Polishing was carried out using 3  $\mu\text{m}$  monocrystalline diamond suspension (Struers DP-Suspension M), and lubricant (Struers DP-Lubricant Red HQ) on a short felt cloth (Struers MD-MOL) followed by final polishing with a 0.05  $\mu\text{m}$  colloidal silica suspension (Struers OP-S) on short felt cloth (Struers MD-CHEM). For the metallographic preparation Buehler Beta manual grinder and polisher were used.

The microstructures of these two kinds of composites were observed using a Nikon Epiphot 200 inverted optical microscope and Phillip scanning electron microscope (SEM) with a detector of backscattered electron detector. Afterward, all samples were tested using a Vickers microhardness unit.

### **3.3.3 Vickers Microhardness**

The ASTM E 384-07 standard test method was used to determine the microhardness of the composites [31]. A Buehler Micromet II digital micro hardness tester was used to perform the microhardness measurement on the composite samples.

### **3.3.4 Analysis of Volume Fraction**

The volume fraction is used frequently in studies of metallurgical systems and phenomena, and at the present project, this measurement was used to calculate the elastic modulus of fabricated composites. Equation 3.1 states the equality of volume fraction to the areal ratio, linear ratio, and point ratio of the selected phase [32]. It has been shown by stereology and quantitative metallography that area fraction is equal to volume fraction [23].

$$V_V = A_A = L_L = P_P \quad \text{Equation 3.1}$$

Area fraction of  $\text{Al}_2\text{Cu}$  and  $\text{AlB}_{12}$  was measured from images taken at 100X, using ImageJ image analysis software (See Appendix).

### **3.3.5 Superficial Rockwell Hardness**

The ASTM E 18-07 standard test method was used to determine the Rockwell hardness and the superficial Rockwell hardness of these materials [33]. The 15T Rockwell superficial hardness test used a 1/16" (1.588 mm) ball indenter and a force of 15 kgf. This method helped determine the overall effect of the microstructure (not just the matrix) on the composite mechanical behavior.

Samples for superficial Rockwell hardness samples were ground on a 320 grit SiC paper to eliminate cutting lines and to secure parallel opposite faces. The samples were cleaned with powdered labware detergent.

### **3.3.6 Differential Thermal Analysis (DTA)**

Thermal analysis comprises a group of techniques in which a physical property of a substance is measured as a function of temperature, while the substance is subjected to a controlled temperature program. In DTA, the temperature difference that develop between a sample and a inert reference material is recorded, when both are subjected to identical heat treatments. The baseline of the DTA curve should then exhibit discontinuities at the transition temperatures and the slope of the curve at any point will depend on the microstructural constitution at that temperature. A DTA curve can be used as a finger print for identification purposes [34].

A DTA curve can be affected by many factors as sample holder, sample mass, heating rate or furnace atmosphere:

- ♦ Sample holder: The geometry, size or heat-sink properties of a sample holder can affect the heat transfer to the center of the sample.
- ♦ Sample mass: The endothermic and exothermic reactions and thermal gradients throughout the sample may have significant effects on DTA results.
- ♦ Heating Rate: The heating rate plays the most important role in DTA. Since thermal degradation is not only dependent on temperature but also on time, thermal degradation of a sample at a higher heating rate will be less because of the shorter time.
- ♦ Furnace atmosphere: The effect of furnace atmosphere on the DTA curve depends on the type of reaction, the nature of the decomposition product and the

type of atmosphere used. Most DTA experiments are conducted under an inert atmosphere, usually nitrogen. Nitrogen increases sensitivity because it is a relatively poor thermal conductor. Other inert gas, such as helium can be used. This has a higher thermal conductivity than nitrogen, and helium can reduce its thermal resistance and increase the resolution of thermal transitions.

A Mettler Toledo TGA/SDTA 851<sup>e</sup> was used to measure the thermal evolution of the composites upon heating and cooling under a nitrogen atmosphere. A seven milligrams sample in alumina crucible of 30 $\mu$ L was used for this analysis in a nitrogen atmosphere with 20 mL/min of flow. The heating cycles were carried out at 10°C/min from 25°C to 750°C, followed by a cooling cycle from 750°C to 25°C at -10°C/min.

### **3.3.7 X-Ray Diffraction (XRD)**

The bulk XRD samples were prepared as solid pieces using a Buehler Isomet low speed saw, and then ground manually with a 1200 grit SiC paper and water as the coolant/lubricant, washed with powdered labware detergent and cleaned with ethanol solution. The diffractometer was operated at 40 kV and 44 mA with a metallic target of Cu  $K\alpha$  radiation, which emit strong x-ray of 1.54 Å.



### 3.3.8 XRD + Differential Scanning Calorimeter (DSC)

The XRD DSC samples had the same pan size, 5x5 mm and 0.2 mm of thickness; in test performance the pan was removed.

The Rigaku Ultima III XRD with Thermo plus XRD DSC II attachment was used to anneal the samples and analyze the peak intensity changes while the diffractograms were recorded *in situ* under nitrogen atmosphere (Figure 3.5). The annealing was set to 300°C for 2 hours with heating rate 20°C/min (max) and the diffractometer parameters were set from  $2\theta=5^\circ$  to  $40^\circ$  with 9 deg/min of scan speed.

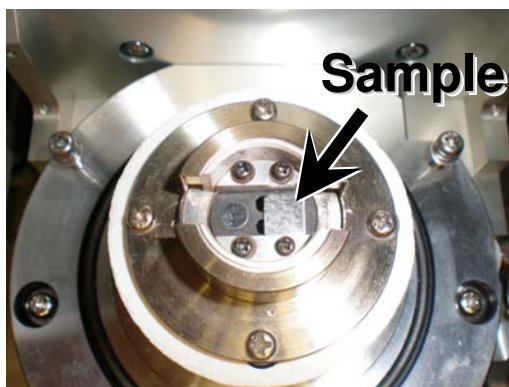


Figure 3.5 XRD DSC chamber with a composite sample.

### 3.3.9 High Temperature XRD

The samples for the high temperature XRD were machined to match the black quartz sample plate size: 13x5 mm and 0.2 mm of thickness. The composites melting process was studied using the Rigaku Ultima III XRD with programmable temperature controller PTC-30 (Figure 3.6). The temperature controller was set with a heating rate at 50°C/min (max) to reach 800°C holding the temperature for 2 hours.

The diffraction test parameters were  $2\theta$  between  $10^\circ$  -  $100^\circ$  and 9 deg/min of scan speed. The tests were completed under a nitrogen atmosphere. Although the XRD patterns were registered before, during and after heat treatment, in this section just patterns recorded before and after the melting tests will be shown, because the melted aluminum signal was noisy and it hid room temperature patterns.



Figure 3.6 Rigaku XRD executing a high temperature test.

## **4 ANALYSIS AND DISCUSSION OF CHARACTERIZATION OF AIB<sub>12</sub>/Al-Cu ALLOYS COMPOSITES**

### **4.1 Bulk Density**

The composites density was calculated from the specific gravity determined using the Archimedean principle. Equation 4.1 shows the specific gravity calculation [35].

$$\rho = \frac{W(a) \cdot \rho(fl)}{W(a) - W(fl)} \quad \text{Equation 4.1}$$

where:

$\rho$  : Specific gravity of the solid

$\rho(fl)$ : Density of the liquid

W(a): Weight of the solid in air

W(fl): Weight of the solid in liquid

The effect of the applied pressure on the sample density is presented in Figure 4.1. The lower points in the plot indicate that the applied pressure was not enough to counteract the inherent porosity of these Al-B-based composites.

When these results are compared with the density of specimens fabricated using gravity casting, it becomes apparent that bulk density of the squeeze cast specimen increased in both composite compositions. In the 2 wt.% Cu specimen, the density had a slight increase from 2.7178 to 2.7183 g/cm<sup>3</sup> and in the 4 wt.% Cu specimen the density increased from 2.7549 to 2.7643 g/cm<sup>3</sup>. Although the density is expected to increase continuously with the applied pressure, Figure 4.1 shows a drop in the density at 31 MPa of applied pressure.

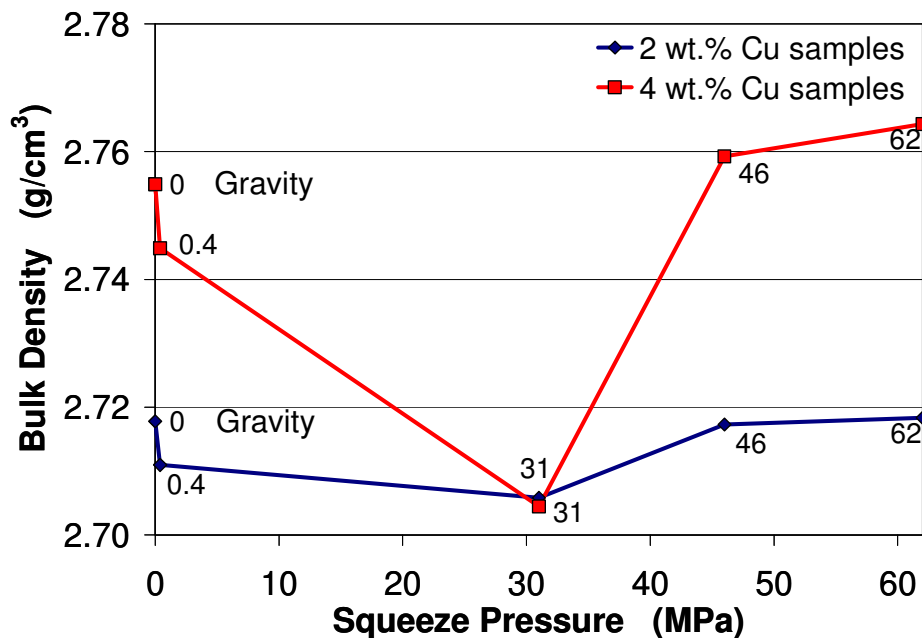


Figure 4.1 Bulk Density of composite fabricated

As known, when the composites are fabricated via gravity casting, shrinkage forms on the top surface and is not accounted for as a part of the internal porosity of the specimens. With low applied squeeze pressure (0.4 and 31 MPa) during the solidification, shrinkage was not counteracted, and formed towards the medium-

section of the specimens. As a result of the applied pressure (not large enough to eliminate the shrinkage), smaller density values were obtained.

Higher applied pressures (46 and 62 MPa) slightly increased the squeezed castings density. With this increment in the applied pressure the shrinkage porosity was practically eliminated and the density approached its theoretical value. According to the results of bulk density measured, it was reasonable to assume that at the pressures of more than 50 MPa they were able to eliminate shrinkage porosity in both composites (2 and 4 wt% Cu).

## 4.2 Microstructural Characterization

Figure 4.2 (a) presents the resulting microstructures with  $\text{AlB}_{12}$  reinforcements embedded in the aluminum matrix and  $\text{Al}_2\text{Cu}$  ( $\theta$ ) phase in the matrix grain boundaries. Additionally, small and fewer particles of  $\text{AlB}_2$  were identified in some samples (Figure 4.2 (b)).

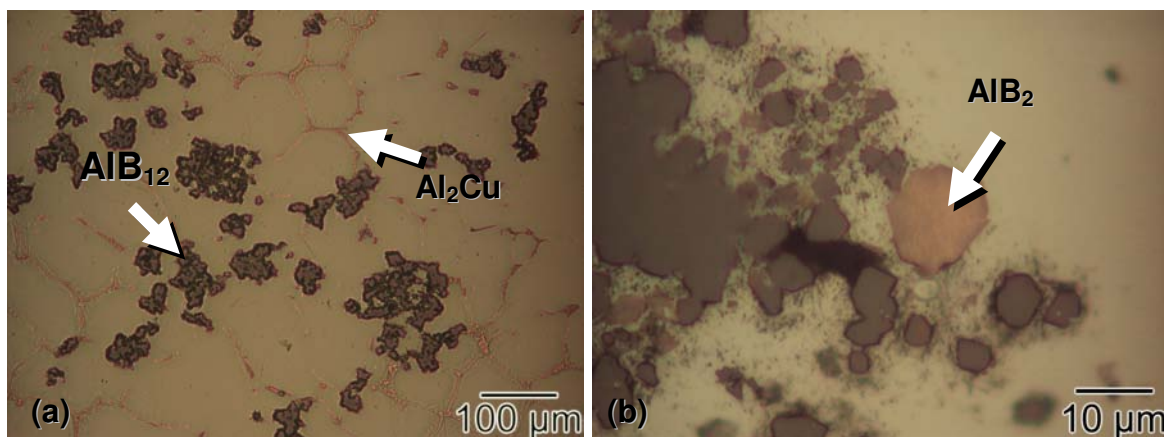


Figure 4.2 Observed phases in composites.

(a) 4 wt.% Cu sample fabricated with 62 MPa of squeeze pressure, cut at 10 cm of specimen bottom.

(b) 2%Cu sample fabricated with 62 MPa at bottom specimen.

Optical microscopy also allowed observing the segregation of the  $\text{Al}_2\text{Cu}$  ( $\theta$ ) phase onto the upper sections in the squeezed specimens. Figure 4.3 shows the distribution of  $\text{Al}_2\text{Cu}$  ( $\theta$ ) phase from bottom to top section the same specimen.

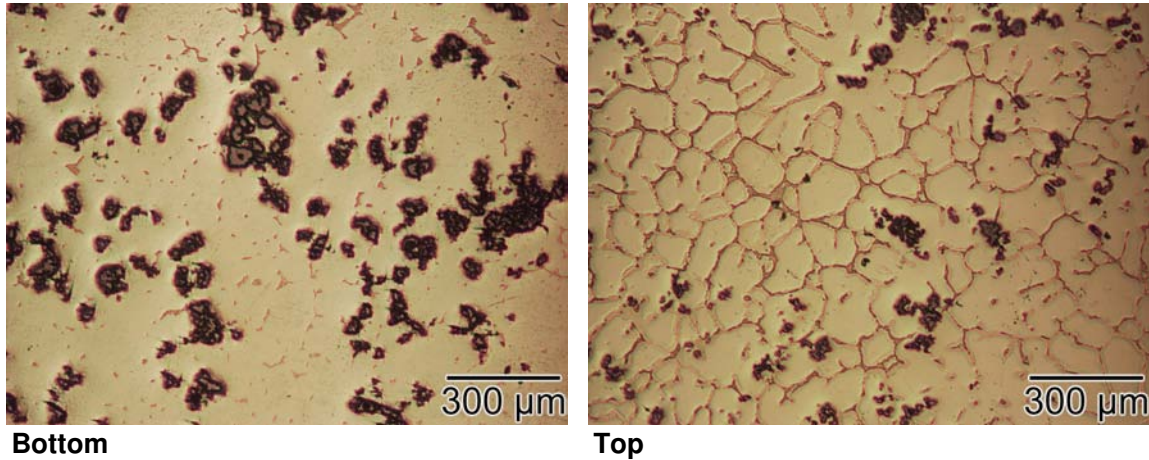


Figure 4.3 Optical micrographs from the bottom and top sections of the squeezed cast 4 wt.% Cu specimen fabricated with 62 MPa.

As a consequence of the applied pressure, some intergranular cracks were formed at mid-length of some samples, as shown in Figure 4.4. However, the crack propagation was stopped by the  $\text{AlB}_{12}$  reinforcements (Figure 4.4 (c)). It is believed that the solidification shrinkage could not be counteracted by lower applied squeeze pressures (0.4 and 31 MPa). Conversely, the shrinkage was reduced when higher squeeze pressures (46 and 62 MPa) were applied.



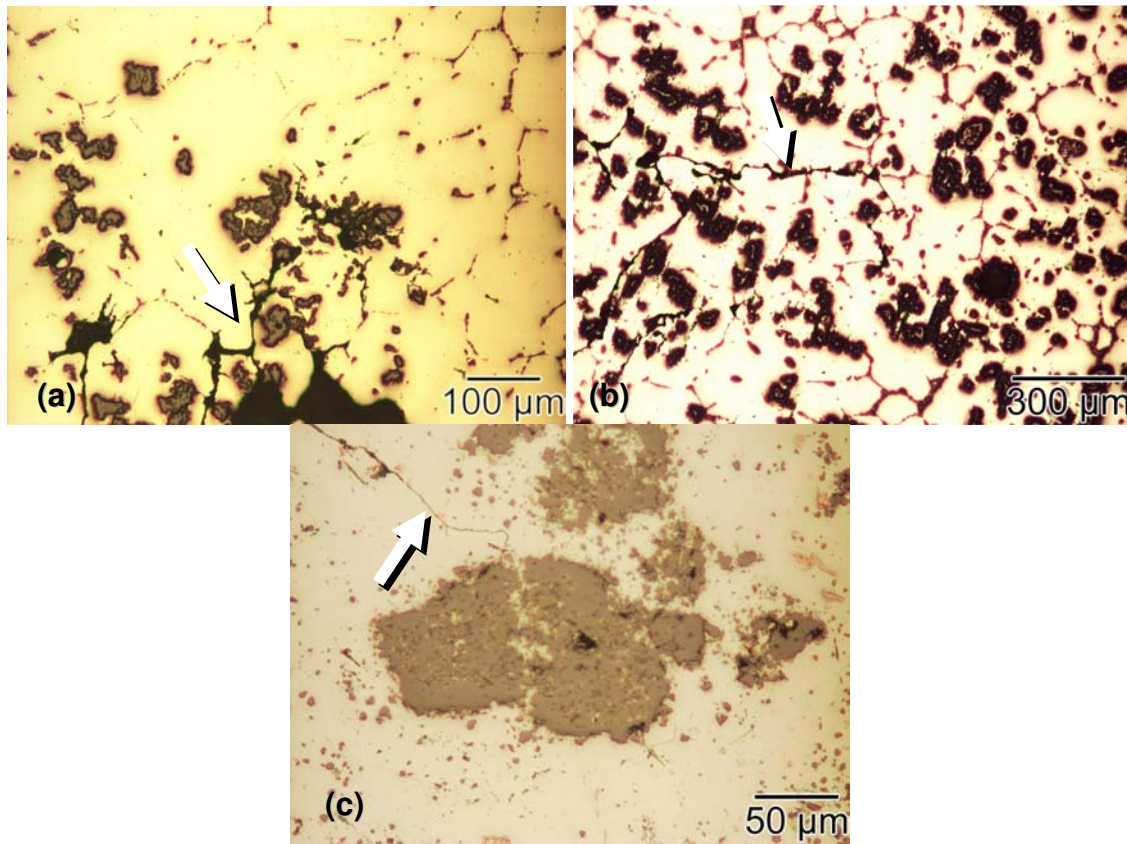


Figure 4.4 Micrographs of cracks observed.  
(a) 2 wt.% Cu specimen squeezed with 31 MPa, obtained at 2.5 cm from the casting bottom.  
(b) 4 wt.% Cu specimen squeezed with 31 MPa, obtained at 10 cm from the casting bottom.  
(c) 2 wt.% Cu specimen squeezed with 0.4 MPa, obtained at 5.0 cm from the casting bottom.

The backscattered electron imaging (BEI) allowed detecting atomic number contrast between areas with different chemical compositions, especially when the average atomic number of the various regions is different. The phases observed initially by optical microscopy were confirmed using BEI. The effective atomic numbers ( $Z_{\text{eff}}$ ) [36] were 6.65 and 21.17 for  $\text{AlB}_{12}$  and  $\text{Al}_2\text{Cu}$  respectively (Figure 4.5 (a)).

BEI was used along with energy dispersive x-ray spectroscopy (EDS) to confirm the presence of boron and aluminum in the  $\text{AlB}_{12}$  reinforcement, as shown Figure 4.5 (b) and (c).

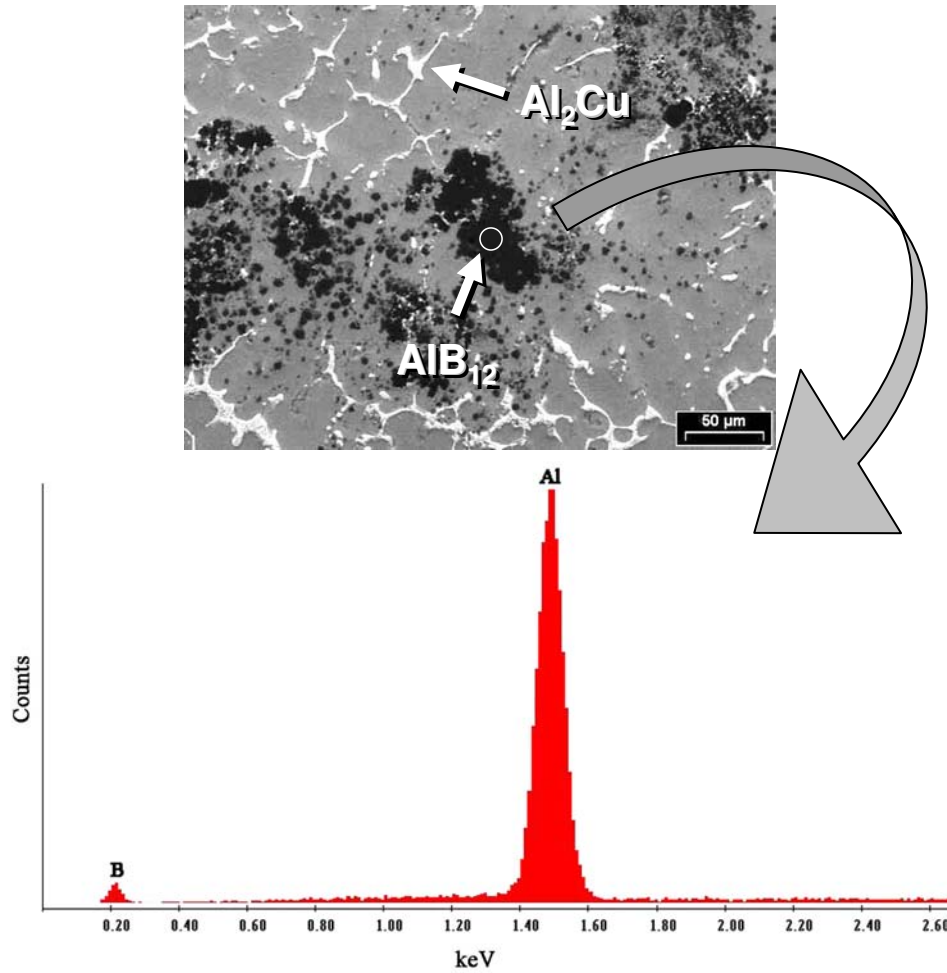


Figure 4.5 EDS analysis from BEI image to an  $\text{AlB}_{12}$  particle.

### 4.3 Analysis of Volume Fraction of $\text{Al}_2\text{Cu}$ and $\text{AlB}_{12}$ Phases

Microstructural features were quantified by calculation of volume fraction from area fraction according to Equation 3.1. Area fraction of  $\text{Al}_2\text{Cu}$  and  $\text{AlB}_{12}$  was



measured from images taken at 100X, using ImageJ image analysis software. The overall volume fraction results of  $\text{AlB}_{12}$  and  $\text{Al}_2\text{Cu}$  are presented in Figure 4.6 where each plotted bar represents the volume fraction average ( $\text{Al}_2\text{Cu}$  and  $\text{AlB}_{12}$  phases) corresponding to each cross section of specimen fabricated with specific composition and pressure.

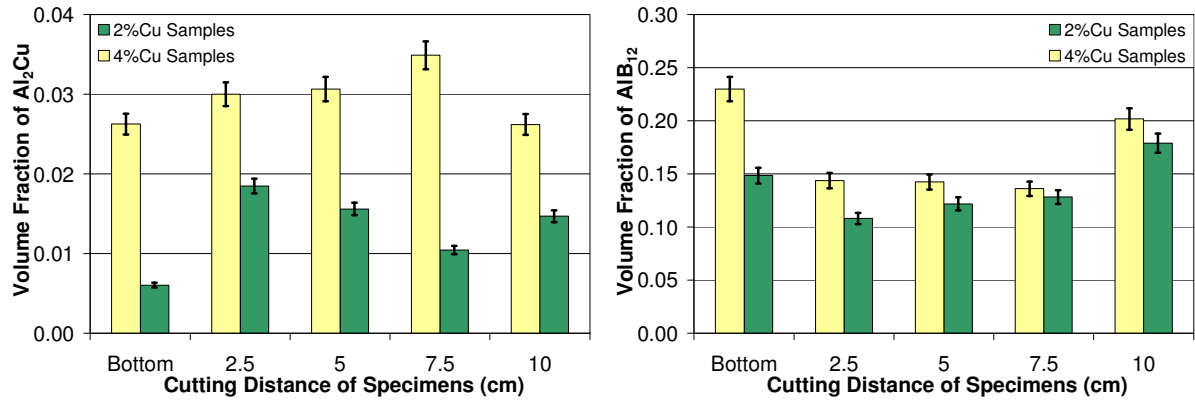


Figure 4.6 Calculated volume fraction of  $\text{Al}_2\text{Cu}$  and  $\text{AlB}_{12}$  phases.

According to these results, the squeeze casting process caused  $\text{Al}_2\text{Cu}$  phase to form preferentially in the upper regions of specimens. When compared with gravity casting samples, the squeezed specimens showed higher amounts of this phase along (1.5 times higher in 2 wt.% Cu samples). This ratio was barely noticeable (0.2%) in the 4 wt.% Cu samples. With respect to reinforcements of  $\text{AlB}_{12}$ , these particles remained preferentially at the end (bottom and top) regions of the specimens, the  $\text{AlB}_{12}$  phase decreasing from bottom to the fourth cutting (at 7.5 cm) of specimens, that was calculated in 13.6% and 40.8% for 2 and 4 wt.% Cu specimens respectively. Additionally, the amount of  $\text{AlB}_{12}$  increased in the last part

at 10 cm; this increment was 39.5% and 48.3% for the 2 and 4 wt.% Cu samples, respectively.

This behavior of  $AlB_{12}$  reinforcement was probably caused by a slower cooling rate at half long region of the specimens. On the other hand, the upper region was the first to solidify and its particles could be retained in the matrix at the levels indicated in Figure 4.6.

With the volume fraction calculation of  $AlB_{12}$  reinforcement, it was possible to determine that the volume fraction average of reinforcement in the fabricated composites was  $15\% \pm 4$ . In addition, the reinforcement size was measured by mean ImageJ image analysis software between 10-100  $\mu m$ .

## **4.4 Vickers Microhardness**

The Vickers hardness value is calculated as follows:

$$HV = \frac{1854.4 P}{d^2} \quad \text{Equation 4.2}$$

where:

d: mean diagonal length of the indentation,  $\mu m$

P: force, gf

A 25 gf load was applied for 30 seconds to perform the test on the aluminum matrix (free of borides and  $\theta$  phase) of the composites, resulting in a average 35.5 HV value for the 2 wt.% Cu samples and 42.3 HV for 4 wt.% Cu ones.

In both composites the highest applied squeeze pressure (62 MPa) appeared to barely increase the matrix hardness, as observed on the Figure 4.7 The mean Vickers microhardness of squeezed specimens was 38.5 HV for the 2 wt.% Cu specimen and 48.7 HV for the 4 wt.% Cu specimen. In general, Vickers microhardness of squeezed specimens was slightly lower than the measurements of the same composites fabricated via gravity casting. For the highest squeezed pressures (46 and 62 MPa) the average microhardness was equal to that measured on the gravity casting specimens.

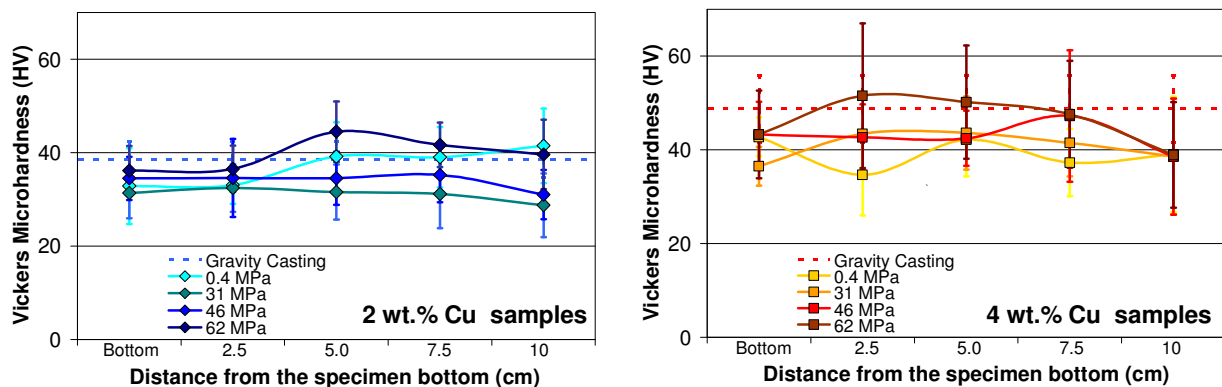


Figure 4.7 Vickers microhardness (HV 25gf/30s) values measured on the matrices of the AMCs fabricated with different squeeze pressures and both 2 and 4 wt.% Cu.

The specimens fabricated with 62 MPa of squeeze pressure had a matrix with the highest microhardness than the other samples. This behavior was due to the

applied squeeze pressure during the matrix solidification likely introduced higher dislocation densities that result in a stronger matrix.

## 4.5 15T Superficial Rockwell Hardness

Figure 4.8 shows superficial Rockwell hardness of composites fabricated via squeeze casting and gravity casting as a function of the distance along the specimens. In this figure the 4 wt.% Cu squeezed specimens showed higher superficial hardness than the 2 wt.% Cu squeezed specimens with 63 HR15T. This evidences the hardening effect of higher contents of copper. The higher pressure caused the reinforcements to redistribute throughout the specimen. Seemingly, these differences in distribution caused a non homogeneous composite material with superficial hardness variations.

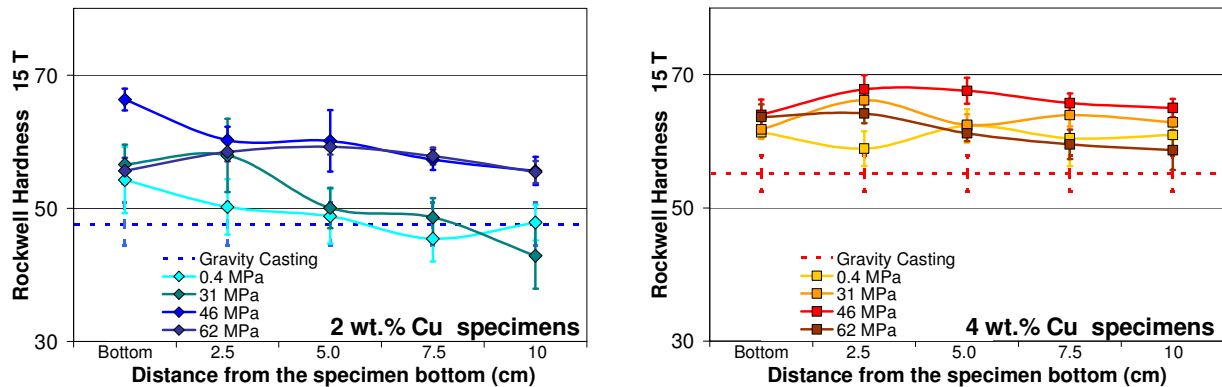


Figure 4.8 Superficial Rockwell hardness (15T) values measured on AMCs fabricated with different squeeze pressures and both 2 and 4 wt.% Cu.

Evidently the superficial Rockwell hardness was improved with the implementation of squeeze casting as a fabrication method. In the 2 wt.% Cu

specimens, the superficial hardness increased 14.4% and in the second set of 4 wt.% Cu specimens the increment was 14%, in both cases with respect to superficial hardness of gravity casting samples. This behavior showed that the superficial hardness was greatly affected by applied squeeze pressure. This is due likely to the enhancement of solubility of solute atom as Cu and B and the decreasing of shrinkage porosity by applied pressures.

## 4.6 Differential Thermal Analysis (DTA)

The DTA curves exhibited two endothermic peaks during the heating cycle. The first peak (at lower temperature) corresponded to a *eutectic* reaction (solidus line) and the second one to the matrix melting point (liquidus line) of the matrix. These temperatures do not correlate exactly with the phase diagram of Figure 4.9.

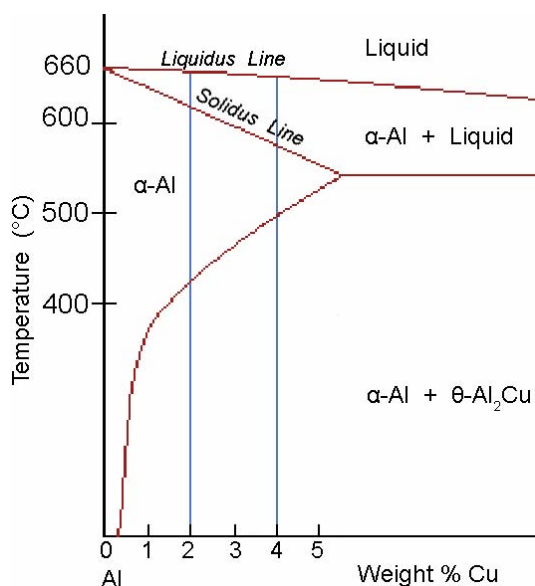


Figure 4.9 Phase diagram Al-Cu.

This behavior can be explained as follow: the total amounts of aluminum in the composites were 91.6 and 93.3 wt.% for 2 and 4 wt.% copper specimens respectively. However, a small amount of aluminum is present in the  $\text{AlB}_{12}$  reinforcement. Then, the aluminum and copper levels in matrix were increased and the locations of both Al-Cu alloys in phase diagram were displaced to the right, from 4 wt.% Cu to 4.22 and from 2 wt.% Cu to 2.10.

The thermal event due to the first reaction was only observed in the 4 wt.% specimens at  $542 \pm 1.2^\circ\text{C}$  (Figure 4.10). This temperature was stable in all samples and represents the eutectic reaction (solidus line):  $\alpha\text{-Al} + \theta \rightarrow \text{Liquid}$ . Additionally, this reaction was confirmed by mean of microstructure of these samples taken at 1000X, the eutectic phase was identified at grain boundaries (Figure 4.11). The recorded temperature was slightly lower than solidus line of the Al-Cu phase diagram, subsequently this behavior confirm for a second time that the Al-Cu phase diagram of this matrix was shifted to the left (Figure 4.9). Table 4.1 shows the differences between the obtained temperatures in the DTA (heating and cooling) and from the literature.

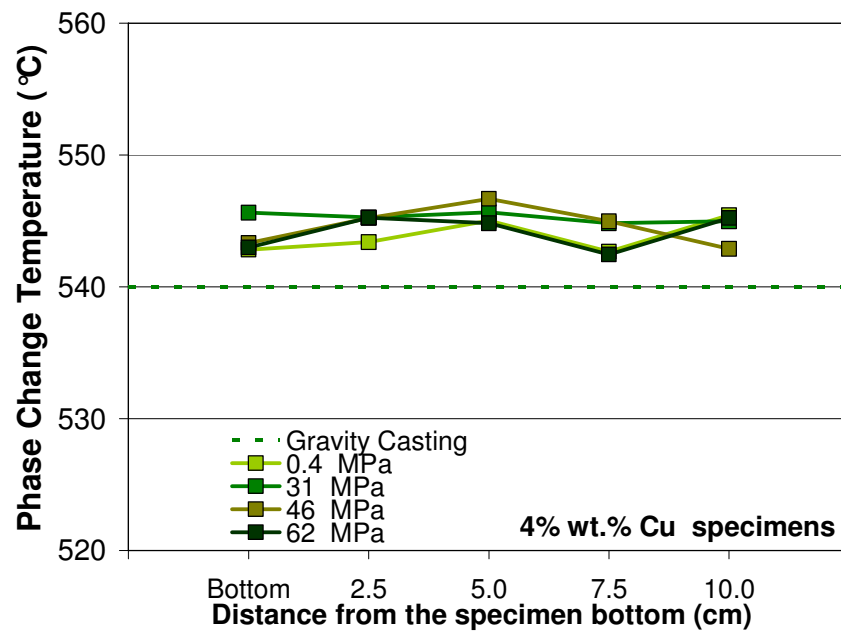


Figure 4.10 Phase change of all analyzed 4% Cu samples.

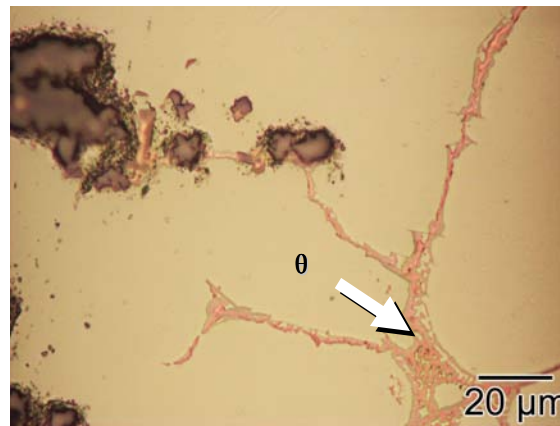


Figure 4.11 Eutectic phase observed in 4 wt% Cu samples.

Table 4.1 Comparative chart of phase change signal (by heating and cooling) and solidus line of reference.

Specimens	Phase Change (solidus line) for Heating by DTA Onset (°C)	Phase Change (solidus line) for Cooling by DTA Onset (°C)	Eutectic Temperature (solidus line) (°C) [37]
4.22 wt.% Cu in matrix	542	541	548

The  $\text{Al}_2\text{Cu}$  ( $\theta$ ) phase formed preferentially on the top regions of the specimens, consequently, the melting points of the top samples were shifted to the left in the DTA curves (lower temperature). Figure 4.12 shows the tendency described previously for a specimen fabricated by 46 MPa of squeeze pressure. The first derivative plots were used to detect and confirm the thermal events like melting points or other phase changes.

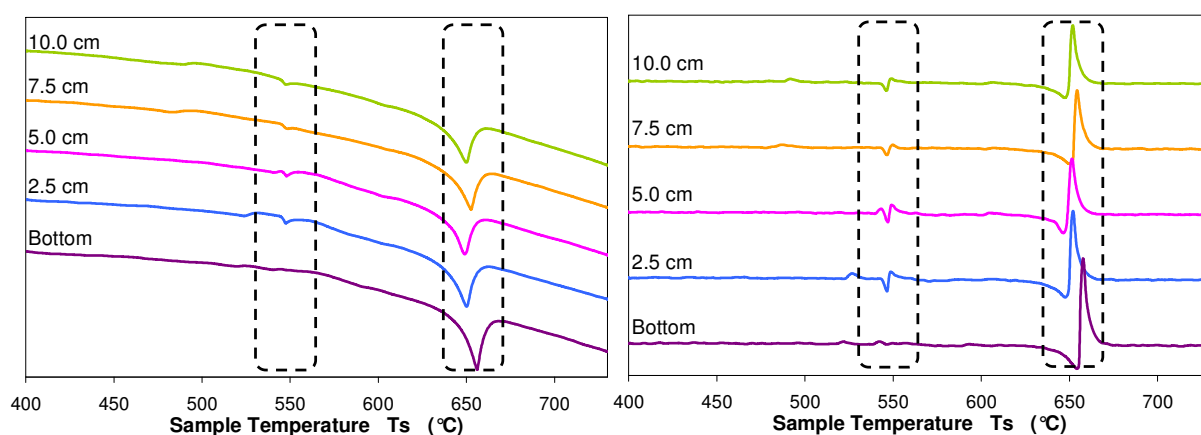


Figure 4.12 DTA and 1<sup>st</sup> Derivative curves of 4 wt.% specimen fabricated with 46 MPa of squeeze pressure.

The highest squeeze pressures (31 - 62 MPa) increased the melting point in all bottom regions of the specimens, as the DTA curves show in Figure 4.13. According to the Al-Cu phase diagram, that behavior indicates Al-rich matrix in the bottom regions of both specimens. The melting reactions by DTA onset were identified and averaged to 648°C for the 2 wt.% Cu specimens and 639°C for the 4 wt.% Cu specimens. These temperatures were slightly lower than expected according to the Al-Cu phase diagram (Table 4.2).



The average melting point of the matrix of the squeezed specimens was evidently higher than the melting points of the specimens fabricated via gravity casting. This increment was calculated as 0.5 and 1.4% for 2 and 4% Cu specimens, respectively. In addition, in Figure 4.13 there is a perceptible slope between bottom and the rest of squeezed specimens. This slope was calculated and averaged for specimens fabricated only with highest squeeze pressures (31, 46 and 62 MPa) to  $-3.5^{\circ}\text{C}/\text{cm}$ . This is equivalent to a melting point difference of 6.2 and 6.4  $^{\circ}\text{C}$  for the 2 and 4 wt.% Cu samples respectively from the bottom to the rest of specimens.

Table 4.2 Comparative chart of melting point, solidification and liquidus line of reference.

Specimens	Melting Point (Heating) by DTA Onset ( $^{\circ}\text{C}$ )	Solidification (Cooling) by DTA Onset ( $^{\circ}\text{C}$ )	Melting Point (liquidus line) ( $^{\circ}\text{C}$ ) [37]
2.10 wt.% Cu in matrix	648	654	655
4.22 wt.% Cu in matrix	639	649	650

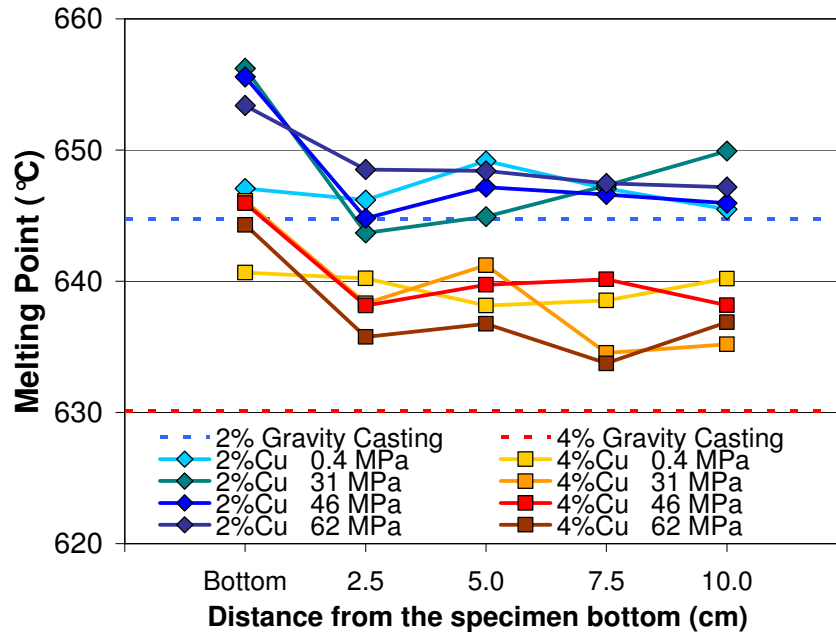


Figure 4.13 Melting points of all analyzed samples.

## 4.7 X-Ray Diffraction (XRD)

### 4.7.1 XRD + Differential Scanning Calorimeter (DSC)

The first aluminum diffraction angle [38] is  $2\theta=38.474^\circ$  for the plane (1 1 1). The same peak was compared for the 5 distances along each specimen. According Figure 4.14, this aluminum peak shifted to the left during heat treatment. This behavior corroborated the thermal expansion of the aluminum unit cell. When the samples were cooled to room temperature after annealing, the aluminum peak returned to its original position.

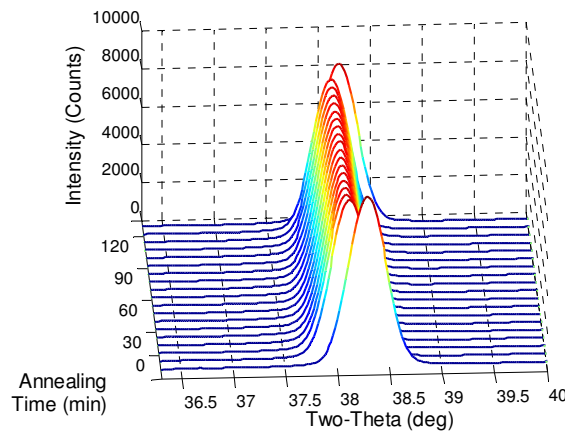


Figure 4.14 XRD Patterns of Al  $2\theta=38.4^\circ$  (1 1 1) at 5 cm from specimen bottom 2 wt.% Cu sample fabricated by squeeze casting with 31 MPa of applied pressure.

The composite matrix (made of aluminum and copper) contained also  $\text{Al}_2\text{Cu}$ , observed by optical microscopy and detected by XRD. The  $\text{Al}_2\text{Cu}$  diffraction peaks within  $2\theta=5 - 40^\circ$  range [39] were  $20.620^\circ$  (1 1 0),  $29.386^\circ$  (2 0 0) and  $37.867^\circ$  (2 1 1). Figure 4.15 shows the first and second  $\text{Al}_2\text{Cu}$  peaks detected and their increasing could be observed. The third  $\text{Al}_2\text{Cu}$  peak at  $2\theta=37.867^\circ$  was not possible

to observe because this peak was overlapped with the aluminum peak at  $\theta=38.474^\circ$  (111). The amount of  $\text{Al}_2\text{Cu}$  increased during the annealing heat treatment due to further stabilization of the microstructure regardless of the presence of borides. This was corroborated during the XRD DSC experiments.

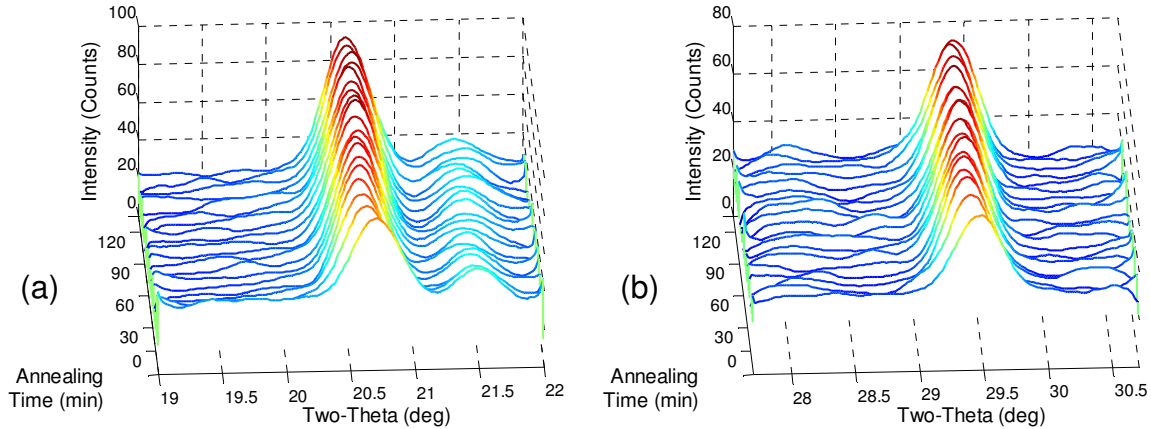


Figure 4.15  $\text{Al}_2\text{Cu}$  peak increasing.

- (a)  $\text{Al}_2\text{Cu}$  peak increasing  $2\theta=20.6^\circ$  at 10 cm from specimen bottom. 2 wt.% Cu sample and 31 MPa of squeeze pressure.  
 (b)  $\text{Al}_2\text{Cu}$  peak increasing  $2\theta=29.4^\circ$  at 5 cm from specimen bottom. 4 wt.% Cu sample and 0.4 MPa of squeeze pressure.

The fabricated composites were reinforced with  $\text{AlB}_{12}$  clusters; according to literature [40] there are 3 reported  $\text{AlB}_{12}$  peaks from  $2\theta=5^\circ$  to  $40^\circ$  with intensity higher than 25%:  $22.607^\circ$  (202),  $36.496^\circ$  (242) and  $36.947^\circ$  (341) all detected by this experiment. Figure 4.16 (a) shows the first  $\text{AlB}_{12}$  peak detected at  $2\theta=22.607^\circ$ , this peak height decreased during heat treatment. The second and third  $\text{AlB}_{12}$  peak at  $2\theta=36.497$  and  $36.947$  were also detected. As these peaks are close together then they were exhibit like one wide peak. This peak is shown in Figure 4.16 (b). A slight left shift during heat treatment was detected, which can be interpreted like a cell size increasing, when the heating was released the peak and

cell came back to  $2\theta$  position and size original, respectively. Also, during the heat treatment, the intensity of this wide peak slightly decreased.

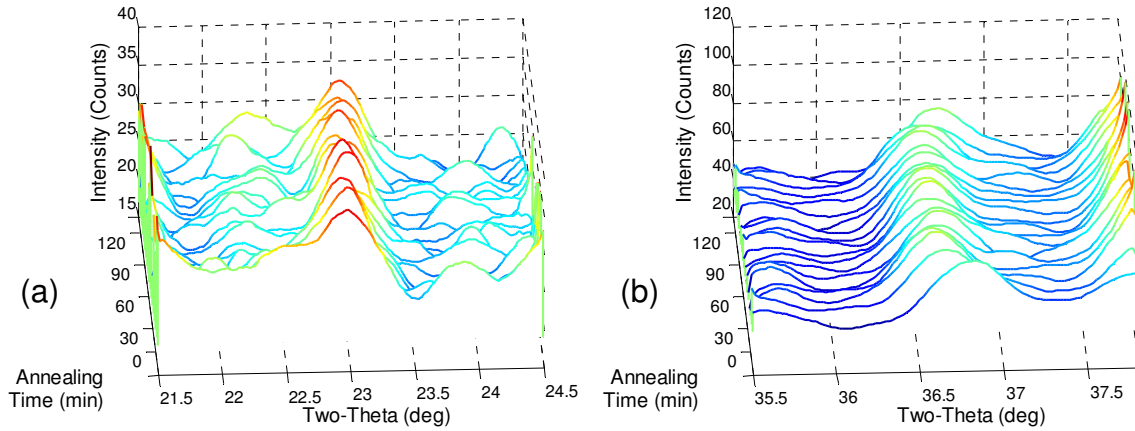


Figure 4.16  $\text{AlB}_{12}$  peak increasing.

- (a)  $\text{AlB}_{12}$  peak increasing  $2\theta=22.6^\circ$  at specimen bottom. 4 wt.% Cu sample and 31 MPa of squeeze pressure.
- (b)  $\text{AlB}_{12}$  peaks increasing  $2\theta=36.5^\circ$  and  $36.9^\circ$  at 10 cm from specimen bottom. 4 wt.% Cu sample and 0.4 MPa of squeeze pressure.

In the fabricated composites some  $\text{AlB}_2$  particles were previously identify by optical microscopy and SEM. This phase was studied in the diffractograms recorded at  $300^\circ\text{C}$  in the XRD DSC. According to the literature [27],  $\text{AlB}_2$  peaks within  $2\theta=5 - 40^\circ$  range were reported at  $2\theta=27.418^\circ$  (001) and  $34.414^\circ$  (100). The  $\text{AlB}_2$  peak at  $\theta=27.418^\circ$  experimented a noticeable intensity increase upon annealing in all samples. Before annealing none of the samples showed the  $27.418^\circ$   $\text{AlB}_2$  peak. This peak appeared and increased in 11.5% of mean during annealing. Figure 4.17 (a) shows the  $\text{AlB}_2$  peak behavior described. The  $\text{AlB}_2$  peak at  $2\theta=34.414^\circ$ , increased slightly in both 2 and 4 wt.% Cu specimens during heat treatment, as shown in Figure 4.17 (b). The increasing of  $\text{AlB}_2$  peaks could be

interpreted as a quantity increasing of  $AlB_2$  phase in both 2 and 4 wt.% Cu specimens during annealing.

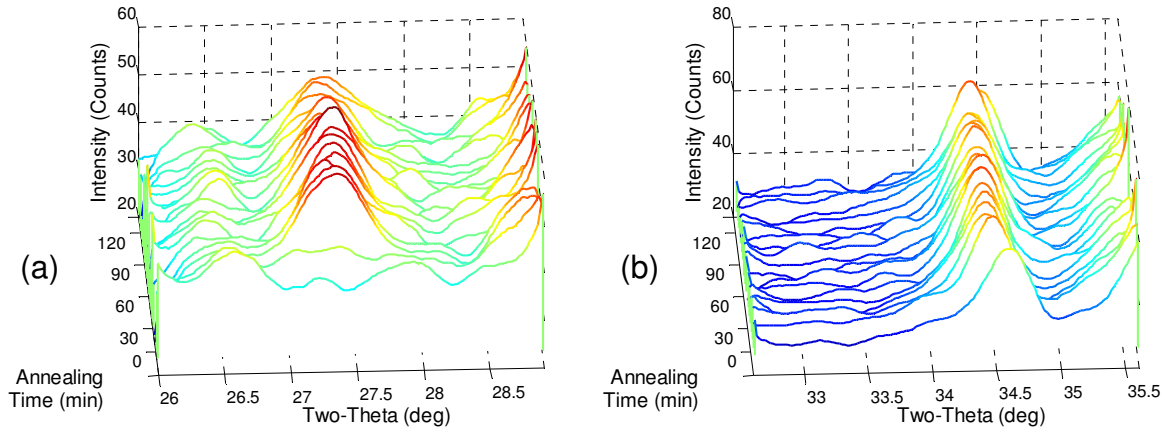


Figure 4.17  $AlB_2$  peak increasing.

- (a)  $AlB_2$  peak increasing  $2\theta = 27.4^\circ$  at 2.5 cm from specimen bottom. 2 wt.% Cu sample and 31 MPa of squeeze pressure.
- (b)  $AlB_2$  peak increasing  $2\theta = 34.4^\circ$  at 5 cm from specimen bottom. 4 wt.% Cu sample and 0.4 MPa of squeeze pressure.

The formation of  $AlB_2$  by decomposition of  $AlB_{12}$  is proved by the slight reduction of  $AlB_{12}$  peak height at  $2\theta = 36.496$  and  $36.947^\circ$  and the appearance and heightening of  $AlB_2$  peaks during heat treatment.

#### 4.7.2 High Temperature XRD

According to the literature [38, 41], there are 6 aluminum peaks for the  $2\theta$  range studied  $38.474^\circ$  (1 1 1),  $44.723^\circ$  (2 0 0),  $65.100^\circ$  (2 2 0),  $78.234^\circ$  (3 1 1),  $82.441^\circ$  (2 2 2) and  $99.190^\circ$  (4 0 0). All these peaks were identified in the XRD patterns. Figure 4.18 shows a XRD pattern from  $2\theta = 10^\circ$  to  $100^\circ$  of a squeezed sample before and after heat treatment. After melting the samples at  $800^\circ\text{C}$  in XRD,

the intensity of aluminum peaks decreased except for the peak at  $2\theta=82.4$  that increased.

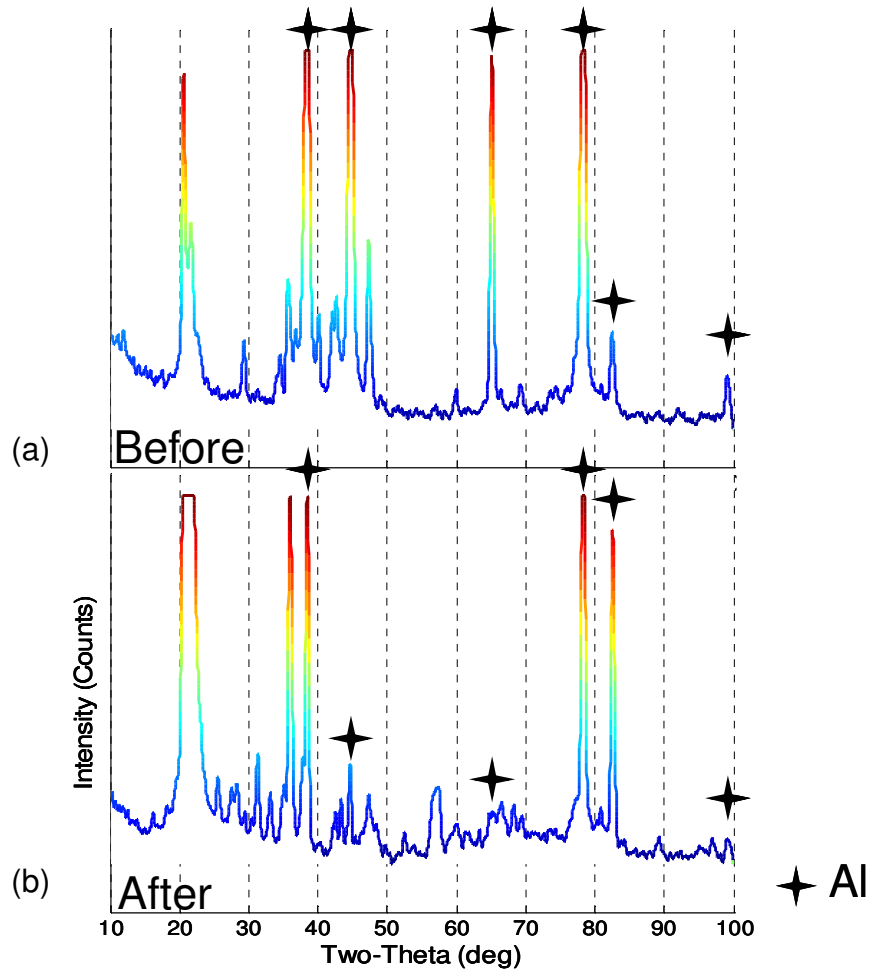


Figure 4.18 XRD patterns of cross section at 5 cm from bottom specimen fabricated with 4 wt.% Cu and 31 MPa of squeeze pressure.

An additional test was conducted in gravity casting specimens; the temperature controller was set to a slow heating rate. The aluminum peaks shifted to the left as in the XRD DSC experiment, and then these peaks vanished when the temperature reached the matrix melting point. Yet, these peaks reappeared when the sample was cooled (Figure 4.19).

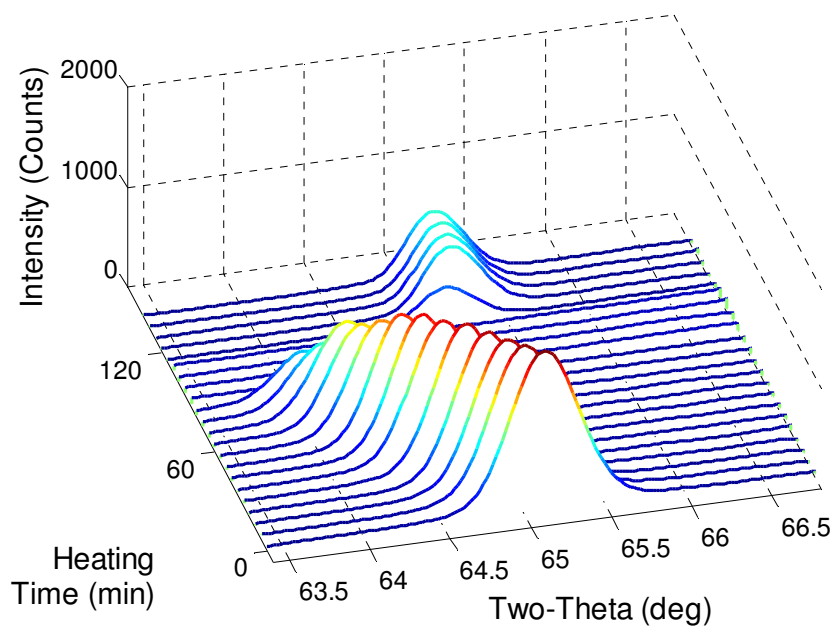


Figure 4.19 Al Peak at  $2\theta = 65.1^\circ$  of (2 0 0).  
Heating slowly to 900°C in reactor X attachment. Gravity casting sample with 4 wt.% Cu.

The  $\text{Al}_2\text{Cu}$  phase was also detected in XRD pattern: at  $2\theta = 20.620$  (1 1 0), 29.386 (2 0 0), 42.591 (1 1 2), 47.332 (3 1 0), 47.808 (2 0 2) and 97.062 (3 1 4) [39]. The first  $\text{Al}_2\text{Cu}$  peak had an important increment, but the other peaks tended to keep the same intensity (Figure 4.20).

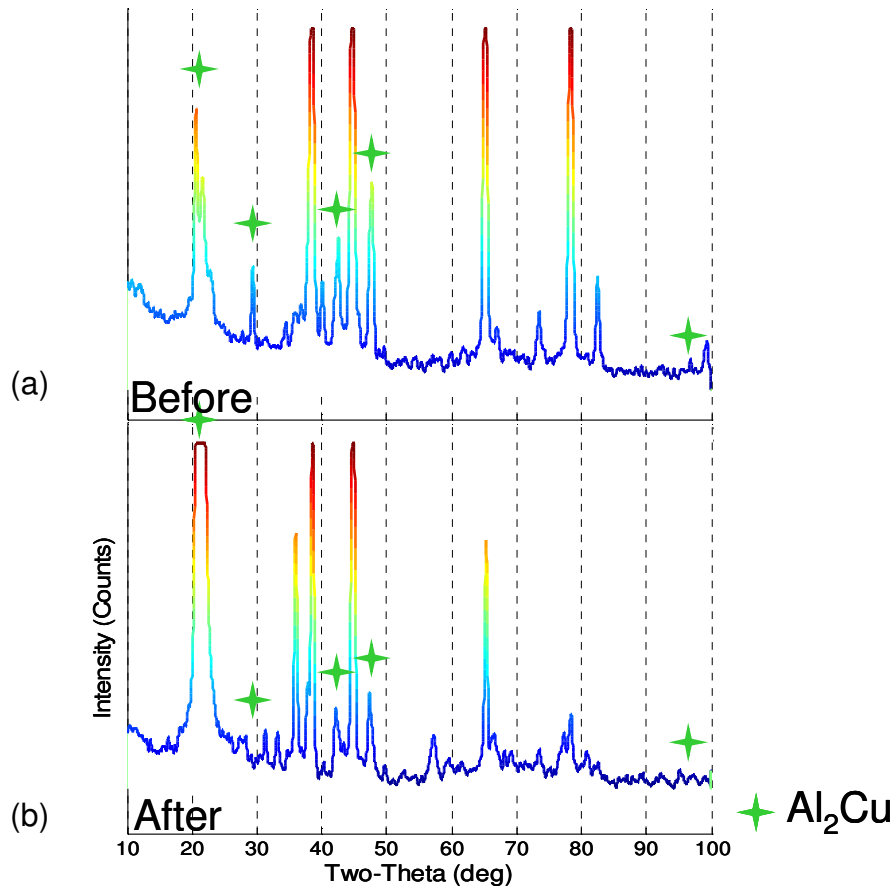


Figure 4.20 XRD patterns of cross section at 10 cm from bottom specimen fabricated with 4 wt.% Cu and 31 MPa of squeeze pressure.

Upon melting, it was very important to study the reinforcement behavior in the composites. The  $\text{AlB}_{12}$  was detected in the XRD patterns, at  $[40] 2\theta = 22.607 (202)$  and  $36.947 (341)$ . The first  $\text{AlB}_{12}$  peak was not easy to identify, because this peak overlaps with the  $\text{Al}_2\text{Cu}$  peak. However, a slight increment of the  $\text{AlB}_{12}$  peak was also determined. The  $\text{AlB}_{12}$  peak increased in both specimens while the second peak decreased (Figure 4.21).



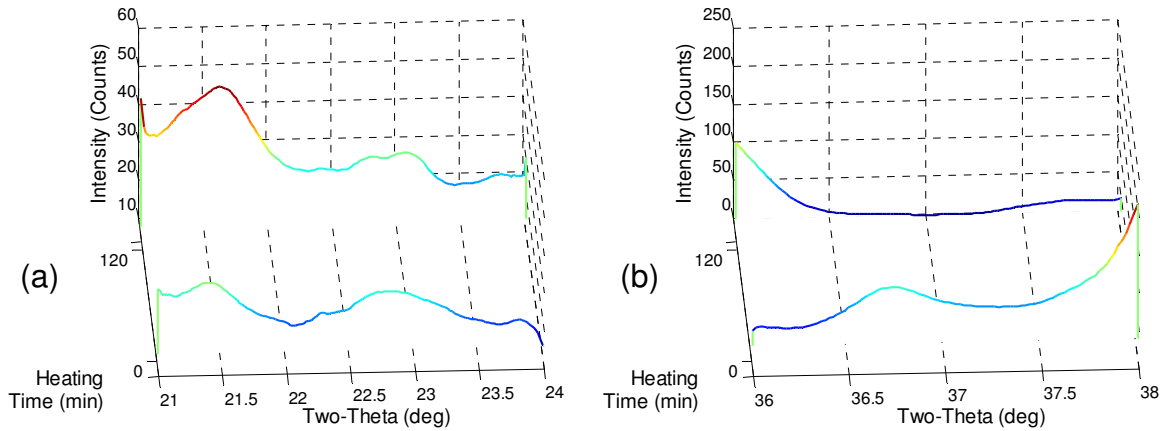


Figure 4.21 AlB<sub>12</sub> peak increasing.

- (a) AlB<sub>12</sub> peak increasing  $2\theta=22.607^\circ$  at specimen bottom. Smelted sample at 800°C hold 2 hours. 4 wt.% Cu and 0.4 MPa of squeeze pressure.
- (b) AlB<sub>12</sub> peak decreasing  $2\theta=36.947^\circ$  at 2.5 cm from specimen bottom. Smelted sample at 800°C hold 2 hours. 4 wt.% Cu and 31 MPa of squeeze pressure.

AlB<sub>2</sub> detection by optical microscopy and SEM motivated to track the AlB<sub>2</sub> peaks using XRD. According to the literature [27], there are 4 peaks with their intensity higher than 25%:  $2\theta=34.414^\circ$  (1 0 0),  $44.542^\circ$  (1 0 1),  $56.539^\circ$  (0 0 2) and  $61.694^\circ$  (1 1 0). The first AlB<sub>2</sub> peak decreased slightly, while the remaining peaks showed that their intensity increased as shown in Figure 4.22.

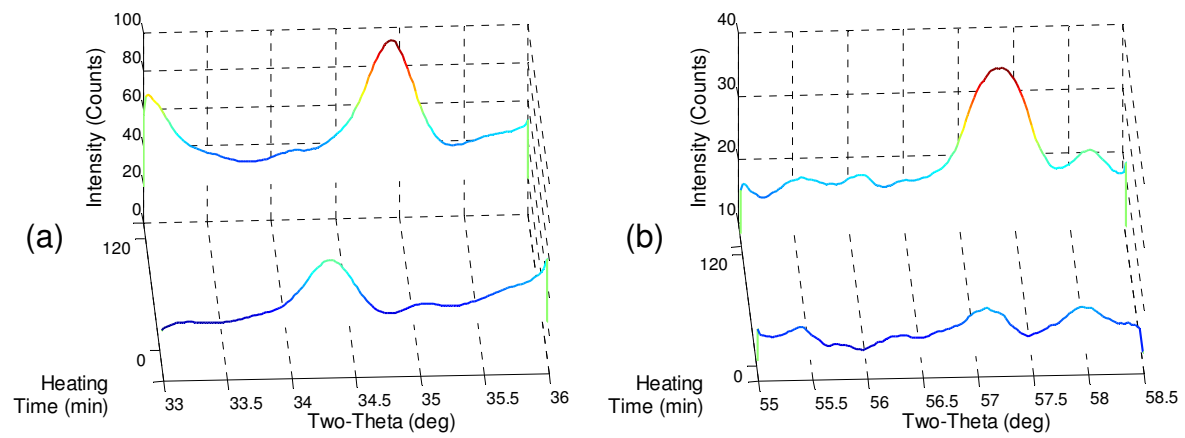


Figure 4.22 AlB<sub>2</sub> peak increasing.

- (a) AlB<sub>2</sub> peak increasing  $2\theta=34.4^\circ$  at 2.5 cm from specimen bottom. Smelted sample at 800°C hold 2 hours. 2 wt.% Cu and 0.4 MPa of squeeze pressure.
- (b) AlB<sub>2</sub> peak increasing  $2\theta=56.5^\circ$  at the specimen bottom. Smelted sample at 800°C hold 2 hours. 4 wt.% Cu and 0.4 MPa of squeeze pressure.

## **5 CONCLUSIONS**

As a result of the squeeze casting process, the manufactures composites had better mechanical, micro and macrostructural characteristics compared with the conventionally processed ones via gravity casting. The key to this task was the control of the processing variables. The most important squeeze casting process parameter that affected the quality of castings was the intensity of applied pressure. Effects of this parameter on the density, microhardness, superficial hardness, differential thermal analysis and x-ray diffraction of  $\text{AlB}_{12}/\text{Al}$  composites were investigated in this work.

The bulk density of the squeezes specimens presented a slight increase due to the applied pressure. The bulk densities measured were 2.7178 and 2.7549  $\text{g/cm}^3$  for both 2 and 4 wt.% Cu specimens respectively fabricated via gravity casting. Finally, the bulk density increased to 2.7183 and 2.7643  $\text{g/cm}^3$  in the same composites fabricated via squeeze casting with 62 MPa of applied pressure. This slight increasing in bulk density was caused by the elimination of the shrinkage porosity during processing.

In both composites the highest applied squeeze pressure (62 MPa) slightly increased the matrix hardness. This increment likely corresponds to a higher

dislocation density in the matrix due to the highest pressure (62 MPa) applied during the solidification of the matrix. This also helped to eliminate shrinkage porosity.

The superficial Rockwell hardness was improved with the implementation of squeeze casting as a fabrication method. In the first set of 2 wt.% Cu specimens, the superficial hardness increased 14.4% and in the second set of 4 wt.% Cu specimens the increment was 14%. This noticeable increment was caused by the pressure applied during the matrix solidification of composites; the matrix was forced to fill the piston and to compact itself eliminating the shrinkage porosity producing harder composites.

Differential thermal analysis permitted evaluating the melting process of both sets of specimens fabricated via squeeze casting. The mean melting points were 648 °C and 639 °C for 2 and 4 wt.% Cu specimens respectively. The increment of the melting point of both specimens fabricated via squeeze casting was caused by the increase in applied pressure. The eutectic transformation detected at 544 °C for the 4 wt.% Cu specimen occurred as consequence of the presence of boron which reduces the solubility of Cu in the Al matrix. The pressure effect and boron caused that the eutectic line extended to the left (Al-rich side). The 2 wt.% Cu specimens did not show any eutectic transformation, then the extension of the eutectic line did not reach this composition.

By means of XRD DSC a mean increment of 32.5% in the  $\text{Al}_2\text{Cu}$  ( $\theta$ ) peak intensity was observed during the annealing of samples due to further stabilization of the microstructure regardless of the presence of boron. The formation of  $\text{AlB}_2$  from  $\text{AlB}_{12}$  has been proved by the slight decrease of intensity of the wide peaks of  $\text{AlB}_{12}$  at  $2\theta=36.496$  and  $36.947^\circ$ , and the appearance and increase of  $\text{AlB}_2$  peaks intensity during the annealing process. Similar results were obtained from the high temperature XRD, where the  $\text{AlB}_{12}$  phase was slightly reduced and the  $\text{AlB}_2$  phase was increased. By this way, it was confirmed the presence of both types of reinforcements in the composites fabricated via squeeze casting.

## References



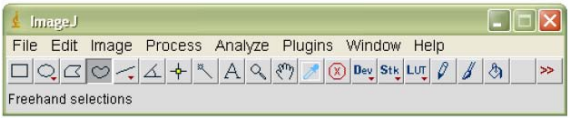
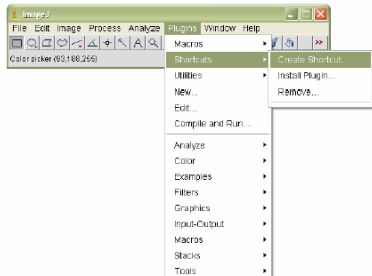
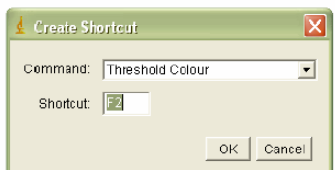
1. Ghomashchi, M.R., Vikhrov, A., *Squeeze casting: an overview*. Materials Processing Technology, 2000. 101: p. 1-9.
2. Crouch, I.G., *Aluminum squeeze casting technology - a European researches viewpoint*. Australian Conference on Materials for Industrial Development, 1987. August: p. 24-26.
3. Mirković, D., Gröbner, Joachim., Schmid-Fetzer, Rainer., *Experimental study and thermodynamic re-assessment of the Al-B system*. Journal of Alloys and Compounds, 2004. 384: p. 168-174.
4. Wang, X., *The formation of  $AlB_{12}$  in an Al-B master alloy*. Journal of Alloys and Compounds, 2005. 403: p. 283-287.
5. Vijayaram, T.R., Sulaiman, S., Hamouda, A.M.S., Ahmad, M.H.M., *Fabrication of fiber reinforced metal matrix composites by squeeze casting technology*. Materials Processing Technology, 2006. 178: p. 34-38.
6. Dorcic, J.L., Verma, S.K., *Squeeze Casting*. ASM Handbook, ed. A. International. Vol. 15 Casting. 1988: ASM International. 323-327.
7. Zhang, M., Zhang, Wei-wen., Zhao, Hai-dong., *Effect of pressure on microstructures and mechanical properties of Al-Cu-based alloy prepared by squeeze casting*. Transactions of Nonferrous Metals Society of China, 2007. 17: p. 496-501.
8. Maleki, A., Niroumand, B., Shafyei, A., *Effects of squeeze casting parameters on density, macrostructure and hardness of LM13 alloy*. Materials Science & Engineering A, 2006. 428: p. 135-140.
9. Maeng, D.Y., Lee, J.H., Won, C.W., Cho, S.S., Chun, B.S., *The effects of processsing parameters on the microstructure and mechanical properties of modified B390 alloy in direct squeeze casting*. Journal of Materials Processing Technology, 2000. 105: p. 196-203.
10. Deshpande, J., *The effect of mechanical mold vibration on the characteristics of aluminum alloys*, in *Manufacturing Engineering*. 2006, Worcester Polytechnic Institute: Worcester, MA. p. 113.
11. Hajjari, E., Divandari, M., *An investigation on the microstructure and tensile properties of direct squeeze cast and gravity die cast 2024 wrought Al alloy*. Materials and Design, 2008. 29: p. 1685-1689.
12. Youn, S.W., Kang, C.G., *Characterization of age-hardening behavior of eutectic region in squeeze-cast A356-T5 alloy using nanoindenter and atomic force microscope*. Materials Science & Engineering A, 2006. 425: p. 28-35.

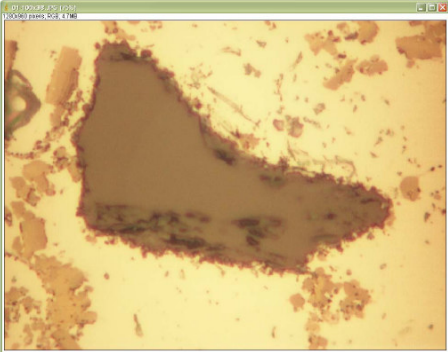
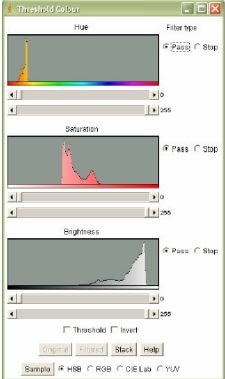
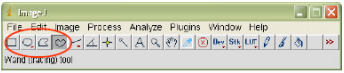

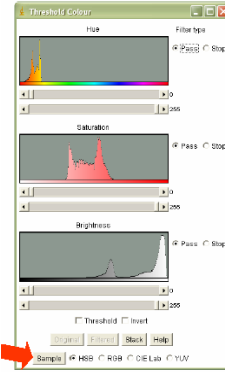
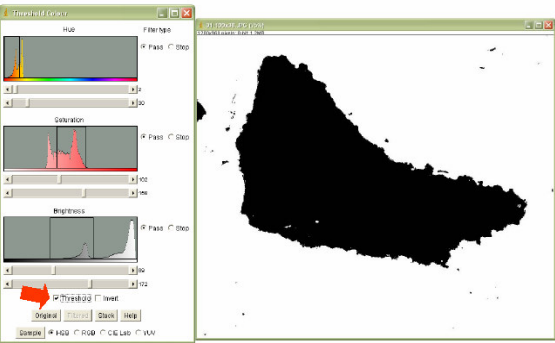
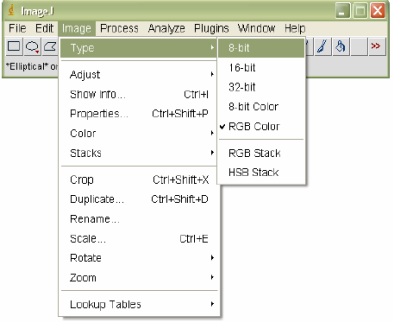
13. Arhami, M., Sarioglu, F., Kalkanli, A., Hashemipour, M., *Microstructural characterization of squeeze-cast Al–8Fe–1.4V–8Si*. Materials Science & Engineering A, 2007.
14. Li, G.R., Zhao, Y.T., Wang, H.M., Chen, G., Dai, Q.X., Cheng, X.N., *Fabrication and properties of in situ (Al<sub>3</sub>Zr+Al<sub>2</sub>O<sub>3</sub>)p/A356 composites cast by permanent mould and squeeze casting*. Journal of Alloys and Compounds, 2008. 471: p. 530–535.
15. Chen, L.G., Shue, K.H., Chang, S.Y., Lin, S.J., *Squeeze casting of SiC<sub>p</sub>/Al-alloy composites with various contents of reinforcements*. Journal Materials Research Society, 2002. Vol. 17, No. 2: p. 376-385.
16. Junk, C.K., Junk, S.W., Nam, H.W., Han, K.S., *Numerical Modeling of Heat Transfer for Squeeze Casting of MMCs*. Journal of Composite Materials, 2003. Vol. 37, No. 6.
17. Callister, W.D.J., *Materials Science and Engineering an Introduction*. 2007, York, PA: Techbooks/GTS. 603-605.
18. Rohatgi, P., *Semisolid Metal Casting and Forging*. ASM Handbook, 1988. 15: p. 327-330.
19. Smagorinski, M.E., Tsantrizos, P. G., Grenier, S., Cavasin, A., Brzezinski, T., Kim, G., *The properties and microstructure of Al-based composites reinforced with ceramic particles*. Materials Science and Engineering A, 1988. 244: p. 86-90.
20. Bhav Singh, B., Balasubramanian, M., *Processing and properties of copper-coated carbon fibre reinforced aluminium alloy composites*. Journal of Materials Processing Technology, 2009. 209: p. 2104-2110.
21. Oñoro, J., Salvador, M.D., Cambronero, L.E.G., *High-temperature mechanical properties of aluminium alloys reinforced with boron carbide particles*. Materials Science and Engineering A, 2009. 499: p. 421-426.
22. Anoop, S., Natarajan, S., Kumares Babu S.P., *Analysis of factors influencing dry sliding wear behaviour of Al/SiC<sub>p</sub>–Brake pad tribo-system*. Materials and Design, 2009.
23. ASM, *Introduction to Alloy Phase Diagram*. ASM Handbook. Vol. 3 Alloy Phase Diagram. 1988, Metals Park, Ohio: ASM International. 1.7-1.29.
24. Okamoto, H., *Al-B (Aluminum-Boron)*. Journal of phase equilibria and diffusion, 2006. 27: p. 195-196.
25. Duschaneck, H., Rogl, P., *The Al–B (aluminum–boron) system*. Journal of Phase Equilibria, 1994. 15 No. 5: p. 543–552.
26. Higashi, I., *Crystal Chemistry of  $\alpha$ -AlB<sub>12</sub> and  $\gamma$ -AlB<sub>12</sub>*. Journal of Solid State Chemistry, 2000. 154: p. 168-176.
27. Wong-Ng, W., McMurdie, H., Paretzkin, B., Hubbard, C., Dragoo, A., NBS (USA). ICDD Grant-in-Aid, 1988.
28. Nafisi, S., Ghomashchi, Reza, *Boron-based refiners: Implications in conventional casting of Al–Si alloys*. Materials and Engineering A, 2007. 452-453: p. 445-453.

29. Ames, L. *Summary information for new high-hardness materials based on AlMgB<sub>14</sub>*. [cited].
30. ASTM, *Standard Test Methods for Density and Specific Gravity (Relative Density) of Plastics by Displacement, Designation: E 792 - 08*. ASTM International, ed. A. International. 2003, West Conshohocken, PA, USA: ASTM International.
31. ASTM, *Standard Test Method for Microindentation Hardness of Materials, Designation: E 384 - 07*. ASTM International, ed. A. International. 2007, West Conshohocken, PA, USA: ASTM International.
32. ASM, *Quantitative Metallography*. ASM Handbook. Vol. 9 Metallography and microstructures. 1985, Metals Park, Ohio: ASM International. 123-134.
33. ASTM, *Standard Test Methods for Rockwell Hardness of Metallic Materials, Designation: E 18 - 07*. ASTM International, ed. A. International. 2007, West Conshohocken, PA, USA: ASTM International.
34. Bhadeshia., H.K.D.H., University of Cambridge. Materials Science & Metallurgy.
35. Sartorius, *Sartorius User's Manual density determination kit Sartorius AG* 2004, Goettingen, Germany: Sartorius.
36. Jayaraman, S., Lanzl, Lawrence H., *Clinical Radiotherapy Physics*. Second ed. Vol. I. 2004, Berlin Germany: Springer. 87.
37. Cambridge, U.o. *Al-Cu phase diagram*. [cited; Available from: <http://www.doitpoms.ac.uk/miclib/pds.swf?targetFrame=Al-Cu>].
38. Swanson, H.E., Tatge, E., Natl. Bur. Stand. (U.S.), 1953. Circ. 539, 1: p. 11.
39. Havinga., L.-C., J.,, Met., 1972. 27: p. 169.
40. Kohn, E., Anal. Chem., 1960. v32: p. 296.
41. Wyckoff, R.W.G., *Cubic Closest Packed, ccp, Structure*. Crystal Structure, 1963. 1: p. 7-83.
42. Wright. *Particle analysis*. 2009 [cited; Available from: [http://www.uhnresearch.ca/facilities/wcif/imagej/particle\\_analysis.htm](http://www.uhnresearch.ca/facilities/wcif/imagej/particle_analysis.htm)].
43. ImageJ. *ImageJ*. 2009 [cited; Available from: <http://rsbweb.nih.gov/ij/docs/menus/image.html>].



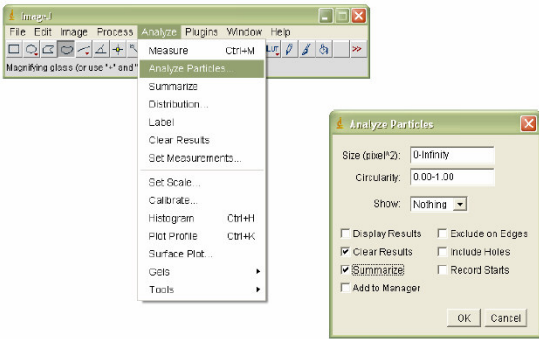
## Appendix

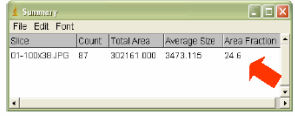
<p><b>1. Why ImageJ ??</b></p> <p>ImageJ is a free software and has more than 300 plug-in</p> <p>Some applications for metallography:</p> <ul style="list-style-type: none"> <li>• Volume Fraction</li> <li>• Reinforcements and Pores</li> <li>• Distances</li> <li>• Matrix Grain Size, Reinforcement Particle size, Indentation Diameter</li> </ul> <p>1</p>	<p><b>2. How to install the ImageJ version 1.41 (2009)?</b></p> <p><a href="http://rsb.info.nih.gov/ij/">http://rsb.info.nih.gov/ij/</a></p>  <p>2</p>
<p>home   news   docs   download   plugins   macros/dev   search   links</p> <p><b>Download</b></p> <p><b>JAR File (Upgrade or Unix)</b> To upgrade to v1.38 or install ImageJ on a Java-enabled machine, download ij138.zip (2MB) and extract the ImageJ directory. Includes Mac and Windows launchers. The Upgrade page has pre-release versions.</p> <p><b>Mac OS X</b> Download ImageJ 1.38 (1.7MB) as a double-clickable Mac OS X application. (Instructions)</p> <p><b>Linux x86</b> Download ImageJ 1.38 (35MB) for Linux x86. Includes the Sun Java 1.5.0_09 runtime and the ImageJ source code. (Instructions)</p> <p><b>Windows</b> Download ImageJ 1.38 bundled with Java 1.6.0_02 (21MB) or without Java (1.7MB). (Instructions)</p> <p><b>Mac OS 9</b> Download ImageJ 1.36 (2.1MB) as a double-clickable Mac OS 9 application. (Instructions)</p> <p><b>Documentation</b> Download the ImageJ documentation (25MB), in HTML format, as a compressed zip archive. The JavaDoc API documentation (567K) is also available.</p> <p><b>Source Code</b> The ImageJ Java source consists of 77,000 lines of code in 242 files. It is available as a zip archive and as colorized and browsable HTML.</p> <p><b>Example Images</b> 31 downloadable sample images and stacks are available in ImageJ's File&gt;Open Samples submenu. These images, and more, are also available as a 8.2MB zip archive.</p> <p>3</p>	<p>The ImageJ icon and its window</p>   <p>4</p>
<p><b>3. How to calculate the volume fraction ??</b></p> <p>You may calculate volume fraction from area fraction to any kind of reinforcement, porous or phases</p> <p>Create the shortcut THRESHOLD COLOUR:</p>  <p>5</p>	<p>Select the Command and assign the function for Shortcut</p>  <p>6</p>

<p>Open the picture or micrograph for analyze: CTRL+O</p> <p>Use preferably images taken to 100X or 200X</p> 	<p>Open the "Threshold Colour" window: F2</p>  <p>Select the region (color) to analyze on picture using tools:</p> 
	<p>Press "Sample" button on "Threshold colour" window:</p>  <p>You can improve the colour selection using "Hue", "Saturation" and "Brightness" bars</p>
<p>Mark "Threshold" box</p> <p>The image colour must change to black and white</p> 	<p>Turn the image to an "8-bit" image (you may create a shortcut)</p> <p>The microscope produces a "RGB color" image format, it is necessary to turn it to a grayscale photograph</p> 

Calculate the volume fraction on "Analyze Particles" (you may create a shortcut)

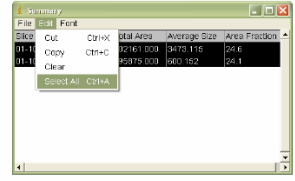
(for our intention, the volume fraction is approximated to area fraction)





You can analyze many pictures

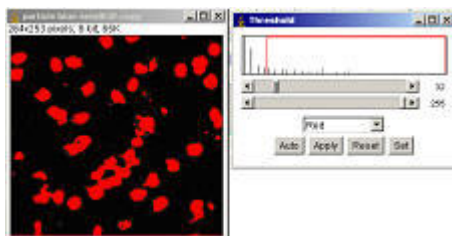
Finally, copy all data ("Select All" and "Copy") and paste it on Excel software



13
14

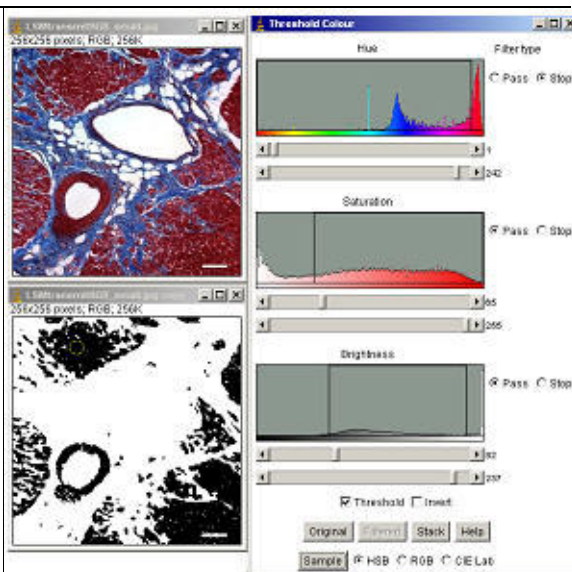
## Setting a threshold [42]

Automatic particle analysis requires the image to be a “binary” image i.e. black or white. The software needs to know exactly where the edges are to perform morphology measurements. A “threshold” range is set and pixels in the image whose value lies in this range are converted to black; pixels with values outside this range are converted to white (or viceversa depending on what the user requests).



There are several ways to set thresholds. For monochrome images it is most simply done via the menu command “*Image/Adjust/Threshold*”. While the threshold is being set, the pixels within the threshold range are displayed in red. The user then changes then “*Apply*” the threshold and the image will be converted to a binary image.

For colour images, setting the threshold is a bit more complicated as each of the red, green and blue channels require different threshold ranges. The plugin “*Plugins/Colour functions/Threshold Colour*” can be used to do this most easily. This opens a fairly complicated and extensive control window. The simplest way to perform a colour threshold is to use one of the selection tools to select one of the objects of interest, and then click the “*Sample*” button in the “*Threshold Colour*” control window. This should remove the pixels in the image that do not have pixels of the same colour as those in the selection. The thresholding can be manually tweaked with scroll bars in the histogram panes. It may be easier to conceptualise what you are doing at this point by switching the Control window from the default Hue, Saturation and Brightness colour model to red, green blue model by switching the option buttons at the bottom of the control window. The image can be displayed as a binary image with the “*Threshold*” button, and converted to a binary image via the menu command “*Image/Type/8-bit*”.



## Type Submenu [43]

Use this submenu to determine the type of the active image or to convert it to another type.

### 8-bit

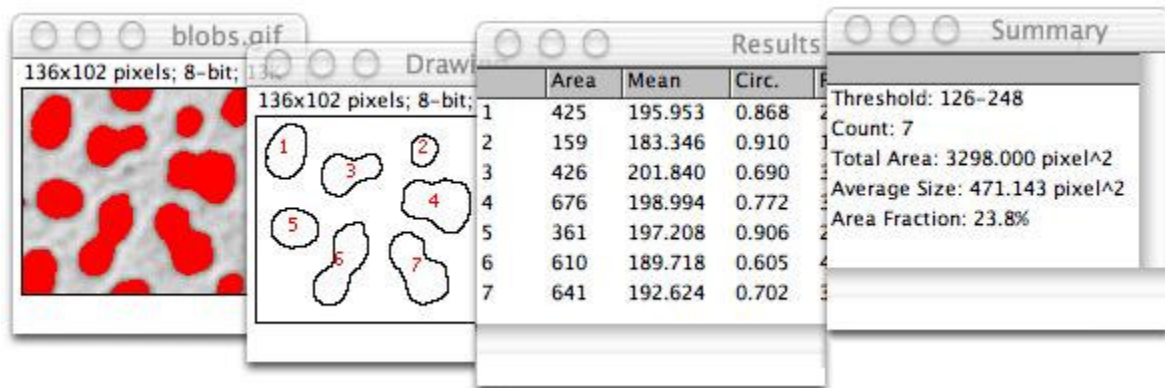
Converts to 8-bit grayscale. The active image must be 16-bit grayscale, 32-bit grayscale, 8-bit color or RGB color.

ImageJ converts 16-bit and 32-bit images and stacks to 8-bits by linearly scaling from min-max to 0-255, where min and max are the two values displayed in the *Image>Adjust>Brightness>Contrast* tool. *Image>Show Info* displays these two values as the "Display range". Note that this scaling is not done if "Scale When Converting" is not checked in *Edit>Options>Conversions*.

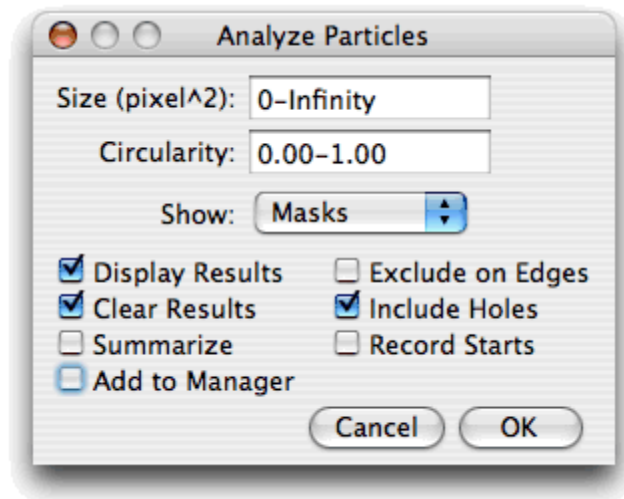
RGB images are converted to grayscale using the formula  $gray = (red + green + blue) / 3$  or  $gray = 0.299red + 0.587green + 0.114blue$  if "Weighted RGB to Grayscale Conversion" is checked in *Edit>Options>Conversions*.

## Analyze Particles [43]

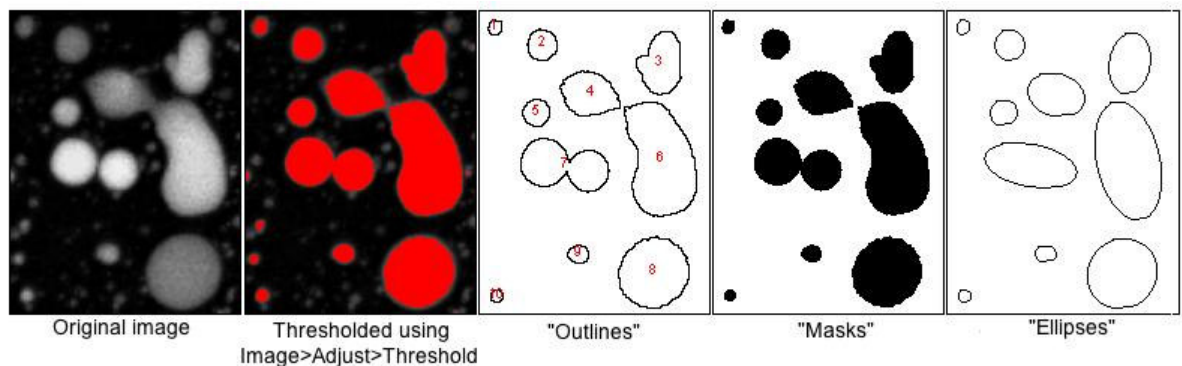
This command counts and measures objects in binary or thresholded images. It works by scanning the image or selection until it finds the edge of an object. It then outlines the object using the wand tool, measures it using the Measure command, fills it to make it invisible, then resumes scanning until it reaches the end of the image or selection. Press the esc key to abort this process. Use *Image>Adjust>Threshold* to threshold an image.



Use the dialog box to configure the particle analyzer. Particles outside the range specified in the *Size* field are ignored. Enter a single value in *Size* and particles smaller than that value are ignored. Particles with circularity values outside the range specified in the *Circularity* field are also ignored. The formula for circularity is  $4\pi(\text{area}/\text{perimeter}^2)$ . A value of 1.0 indicates a perfect circle.



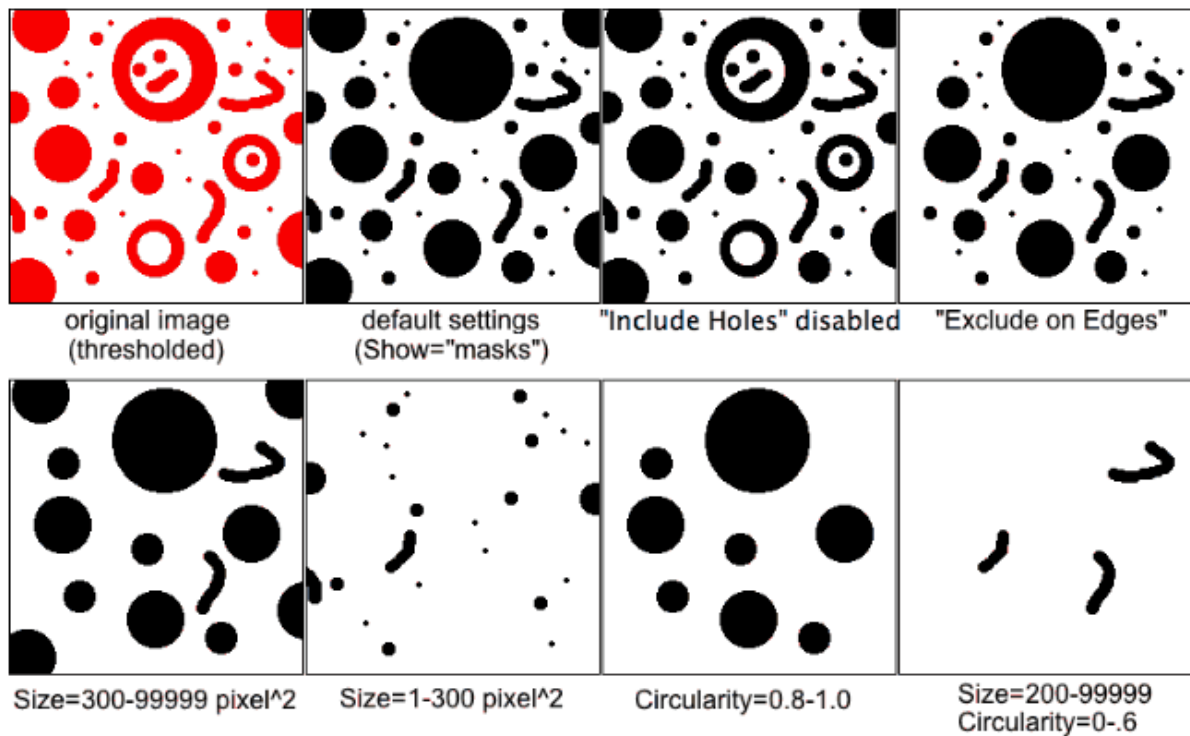
Select *Outlines* from the "Show:" popup menu and ImageJ will open a window containing numbered outlines of the measured particles. Select *Masks* to display filled outlines of the measured particles or *Ellipses* to display the best fit ellipse of each measured particles.



Check *Display results* to have the measurements for each particle displayed in the "Results" window. Check *Clear Results* to erase any previous measurement results. Check *Summarize* to display, in a separate window, the particle count, total particle area, average particle size, and area fraction. Check *Exclude on Edges* to ignore particles touching the edge of the image or selection.

Check *Include Holes* to include interior holes. Disable this option to exclude interior holes and to measure particles enclosed by other particles. When this option is enabled, ImageJ finds the extent of each particle by tracing the outer edge. When it is disabled, ImageJ finds the extent by flood filling.





The *Record Starts* option allows plugins and macros to recreate particle outlines using the `doWand(x,y)` function. The [CircularParticles](#) macro demonstrates how to use this feature.

Check *Add to Manager* and the measured particles will be added to the [ROI Manager](#).